Monitoring Groundwater Flow with Electrical Resistivity Tomography

by

Alexander Van Ballaer

To obtain the degree of Master of Science
At the Delft University of Technology,
To be defended publicly on Friday 21 August, 2020 at 11:00 AM

Student number: 4504429
Project Duration: March 2, 2020 – August 7 2020
Thesis committee: Prof Dr. Ir. E.C. Slob,   TU Delft, Principal Supervisor
Dr. M. Karaoulis,   Deltares, Supervisor
Prof. Dr. F. Wagner,   RWTH Aachen, Examiner
Prof. Dr. D.S. Draganov, TU Delft, Examiner

TUDelft

Abstract

Geophysical monitoring is a popular tool in aquifer characterization and groundwater flow. To address this objective at groundwater extraction site 't Klooster, an ERT dataset was analyzed to identify groundwater flow patterns resulting from the injection of warm oxygenated water. Using a petrophysical model, changes in resistivity were converted to estimated temperature changes to visualize the spread of warm oxygenated water. Multi-dimensional analysis of the resistivity response of the subsurface was carried out. This allowed for the division of the subsurface into 4 depth regimes according to their response to well activity. It is shown that wells up to 100m removed from the ERT set-up influenced the temperature distribution. Furthermore, injected oxygenated water highlighted a preferential flow path between the depths of 20 and 35m in a north-west direction. This is in line with global groundwater flow in the area. Groundwater flow effects could not be reliably separated from the effect of well activity, however its effect is recognized both during extraction of groundwater and injection of warm water.

Acknowledgements

List of Figures

Abbreviations

ERT   Electrical Resistivity Tomography

CHERT   Cross Hole Electrical Resistivity Tomography

SIR   Subsurface Iron Removal

DTS   Distributed Temperature Sensing

R   Model Resolution Matrix

Nomenclature

m   length (meters)

s   time (seconds)

ρ resistivity (Ohm m)

T   temperature (°C)

mg   mass (milligrams)

$Fe^{2+}, Fe(II)$ divalent iron

$Fe^{3+}, Fe(III)$ trivalent iron

M   molar (mol/liter)

S   Siemens (Ohm^{-1})

Contents

1. Introduction

Since its conception in the early 20th century, direct electric current surveying methods have grown to become a popular geophysical tool in the field of hydrogeophysics (Cardarelli et al., 2019). This can be attributed to their speed of surveying, their cost effectiveness, and their extremely wide range of applications. These cover scales ranging from centimeters in laboratory studies to several kilometers for deep earth imaging (Gunther et al., 2012). The introduction of cross-hole electrical resistivity tomography (CHERT) – the placing of electrodes in boreholes rather than only on the surface – allows for the delineation of small-scale features, even at significant depths (Maurer et al., 2009). It has become a robust and flexible tool, used across many disciplines of engineering, agriculture and archaeology. Over the course of the past decades, advances in electrical resistivity tomography (ERT) and the field of inverse theory have made it possible to move on from relatively limited 1D studies, to 2D, 3D and even 4D (time lapse) studies. This makes ERT ideally suited for monitoring dynamic processes in detail. Examples include seasonality studies in the vadose zone, contaminant monitoring, natural hazard monitoring and identifying groundwater flow paths in subsurface aquifers (Hermans et al., 2015). In countries such as the Netherlands, groundwater behavior is extensively monitored and studied (Vries, n.d.). Key driving factors are protection of ecosystems and the adoption of sustainable and economical extraction practices.

1.1 Groundwater in the Netherlands

Fresh water extraction for the purpose of drinking water in the Netherlands totaled 1260 million cubic meters in 2016 and originates from 2 sources. These are: groundwater (includes riverbank filtration water and water stored in dunes) and surface water. Respectively, these make up 65% and 35% of the balance (Dutch Drinking Water Statistics 2017, 2017). Groundwater in the Netherlands is therefore a key source of potable water. It is particularly dominant in the east of the country, and in regions devoid of major surface water bodies such as the IJselmeer Lake or the Drentsche Aa river. Groundwater recovery in the west of the country is complicated by the shallow depth of the saline-fresh groundwater interface, where chloride concentrations exceed 1000mg per liter (Geudens et al., 2017).

Groundwater is naturally filtered from natural and anthropogenic pollutants (Pierzynski, 2015). Due to its depth, it is also somewhat shielded from surface pollutants that often threaten surface water resources. It therefore requires less rigorous purification before it is fit for consumption. A concern with groundwater is that it often contains dissolved impurities like iron (Fe^{2+}). These originate from the natural weathering of iron bearing rocks and minerals. Given that iron is the 4th most common element in the Earth's crust, it is found in nearly all groundwater resources. Iron (as Fe^{2+}) readily dissolves in water with low oxygen content: conditions that are often prevalent in subsurface aquifers (Iron & Manganese in Groundwater, 2007). At naturally occurring concentrations, this is not harmful, but can produce undesirable taste, smell and color. Furthermore, iron in drinking water has staining properties, and can result in the growth of bacteria and other micro-organisms. The latter can be especially problematic in plumbing and drinking water distribution networks, as it has the potential to impede flow (Sharma, 2001). It is therefore in the best interest of drinking water companies to keep concentrations of dissolved iron to a minimum.

1.2 Problem and Research Questions

At certain locations, groundwater is filtered in-situ through a process called subsurface iron removal (SIR) (Jonge et al., 2018). By injection of oxygen rich water into an aquifer, dissolved iron flocculates out of the local groundwater, and is left behind in the aquifer. The iron deficient water is subsequently extracted. This process is explained in more detail in Section 2.2.

This injection-extraction procedure needs to be carried out with consideration. Injecting too much oxygenated water is both costly and inefficient. Injecting too little leaves most of the iron dissolved in the groundwater. This could result in iron flocs forming in the well screens, effectively clogging the well (Karaoulis et al., 2019). Currently, the injection-extraction procedure is determined by the experience of on-site operators. Dutch groundwater companies have expressed a desire to have their operations evolve away from this towards being data driven, in the hope of improving efficiency (Jonge et al., 2018). This involves careful monitoring of the subsurface to determine preferential flow paths of the injected water and to understand the behavior of groundwater in the area.

A recent CHERT study at groundwater extraction site 't Klooster by Deltares (see Karaoulis et al., 2019) shows that injection of marginally warmer (±1°C) oxygen rich water results in small, but discernable resistivity contrasts with local ground water. Only 16 hours of a total of 391 consecutive hours of time lapse ERT data were analyzed. This thesis looks at the entirety of that ERT dataset, with the aim of answering the following research questions:

1) Is it possible to identify preferential flow paths using CHERT data?
2) What is the effect of operating wells far away from the ERT setup on the measured resistivity distribution?
3) Is it possible to separate natural groundwater flow from pumping induced flow?

It has been shown that electrical resistivity is a property that is significantly influenced by temperature (Hermans et al., 2014). If there are no other factors in flux and at a limited temperature interval, changes in resistivity are linearly related to changes in fluid temperature (Hayashi, 2004). Using the petrophysical model outlined in Hermans et al. (2014), changes in resistivity can be converted to changes in temperature. See Section 3.1 for more details. Recently, distributed temperature sensing measurements of the same time period and area were made available. These are compared with the temperature data derived from resistivity measurements. This could serve to verify the accuracy of the ERT results.

2. Preliminary Study

This section provides details on the circumstances of the previously completed geoelectric survey and the inversion of its results.

2.1 Well Field 't Klooster

This thesis is a study surrounding one of Dutch drinking water company Vitens' major groundwater extraction sites: 't Klooster. Here, subsurface iron removal has been a key step in the groundwater filtration process since the station's start of operations in 1965 (Jonge et al., 2018). Drinking water extraction field 't Klooster is located in the Achterhoek, the easternmost part of the Dutch province of Gelderland. The nearest urban area is Hengelo, some 3km to the east. Figure 1 shows the location of the 12 pumping wells, the area from which groundwater is extracted and the surrounding area that is protected. Together, these wells extract between 4.5 million and 4.8 million cubic meters of ground water every year (Grondwateronttrekking en - stroming, n.d.) The well intakes are found at depths between 15m and 37m below surface level or 0m to -22m NAP (Huizer, 2019).

Figure 1: Location of groundwater extraction site 't Klooster. The right image shows the locations of the pumping wells, as well as the area of groundwater extraction and the area designated as protected. From: Folmer et al. (2012)

2.2 Subsurface Iron Removal

't Klooster is one of 6 pumping stations in de Achterhoek where in-situ iron removal is carried out (Jonge et al., 2018). Contrary to conventional above ground filtering procedures, SIR filters out dissolved Fe^{2+} and other undesirable ions prior to extraction. If effective, this process means only minimal filtering above ground is required. This is more economical than filtration in a treatment plant.

Dissolved iron can be removed in several different ways (Sharma, 2001). At 't Klooster, iron removal is performed by oxidation via aeration of the groundwater. Intermittently, oxygen-rich water is injected by one of the 12 on-site pumping wells to promote flocculation of dissolved iron. After some time, the remaining iron-deficient ground water is extracted. Figure 2(a) and 2(b) are simplified schematics of the injection and extraction procedure respectively. Injected oxygen rich water largely displaces the Fe(II) rich groundwater. As it does so, Fe(II) is oxidized at the outer regions of the injection front, consuming dissolved O_2. This results in a lag between the injection and oxygen rich

front. The oxidized Fe forms flocs of trivalent iron oxides(Fe_2O_3) or oxide-hydroxides (FeOOH) that readily adsorb to the matrix particles of the aquifer (sand and gravel) (Braester et al., 1988). The oxygenated water, as well as a volume of water that is now iron deficient is then extracted. As iron rich water transverses the flocculation zone, dissolved Fe(II) adsorbs on to previously adsorbed iron(III) hydroxides (van Halen et al., 2008). When this new layer of iron hydroxides is entirely occupied, any further extracted groundwater will contain significant concentrations of Fe(II) again (Schoonenberg, 2015).
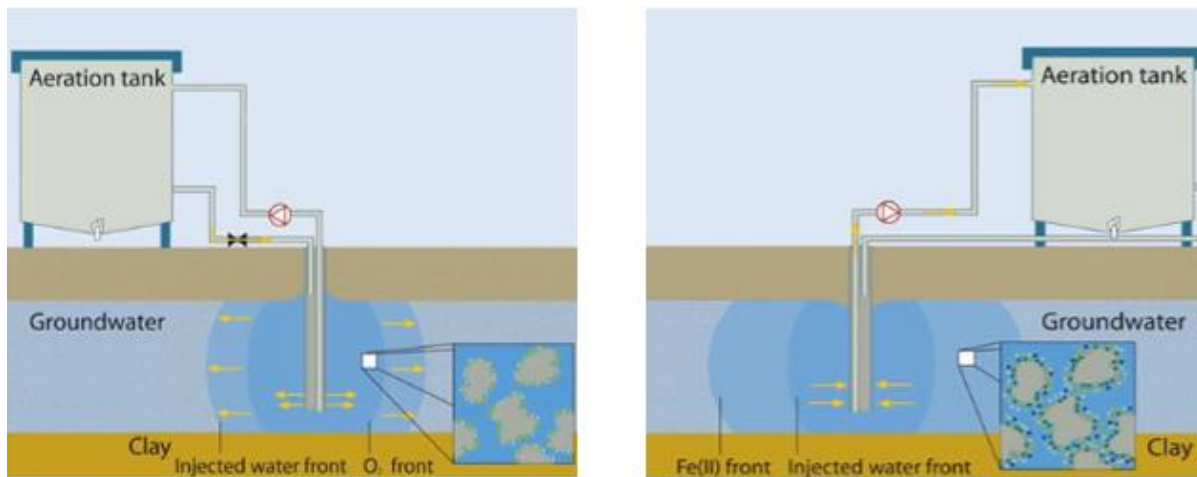
Figure 2: (a), left: Oxygen rich water is injected into an aquifer. The oxygen front lags the injected water front, as O_2 is consumed in the oxidation of Fe(II) to Fe(III). Fe(III) adsorbs on the matrix particles. (b), right: Fe2+ deficient water is extracted. Fe^{2+} ions adsorb on to the adsorbed Fe(III). From: Halem et al. (2008).

This method is relatively cheap, does not involve the use of chemicals, and is straightforward to implement (Sharma, 2001). Schoonenberg (2015) explains how aeration can stimulate the oxidation of iron along 3 distinct pathways. These are: homogeneous iron oxidation, heterogeneous iron oxidation, and biological iron oxidation. Heterogeneous iron oxidation, also known as adsorptive iron oxidation, is the mechanism that dominates during SIR. Therefore, it is expanded on briefly in the next section.

2.2.1 Heterogeneous Iron Oxidation

Heterogeneous iron oxidation in SIR is a 3-step reaction that happens sequentially over time (Schoonenberg 2015).

Step 1: Adsorption

Fe^{2+} ions in the groundwater adsorb to the grains of the aquifer matrix.

$Governing\ Equation: S - OH^0\ +\ Fe^{2+}\ \rightarrow S - OFe(II)^+\ +\ H^+$ (1)

Step 2: Oxidation

In the presence of the injected oxygen, adsorbed iron(II) is oxidized.

$Governing\ Equation: S - OFe(II)^+\ +\ \frac{1}{4}\ O_2\ +\ H^+ \rightarrow S - OFe(III)^{2+}\ +\ \frac{1}{2}H_2O$ (2)
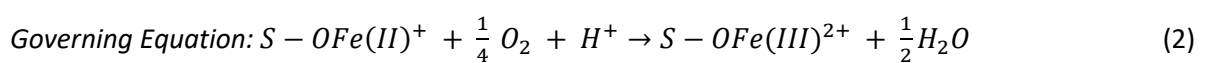
Step 3: Hydrolysis

Adsorbed and oxidized iron is hydrolyzed.

Governing Equation: $S - OFe(III)^{2+} + 2H_2O \rightarrow S - OFe(III)(OH)_2^0 + 2H^+$ (3)

Combined:

$S - OH^0 + Fe^{2+} + \frac{1}{4} O_2 + \frac{3}{2} H_2O \rightarrow S - OFe(III)(OH)_2^0 + 2H^+$ (4)
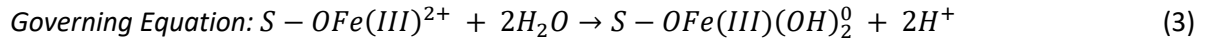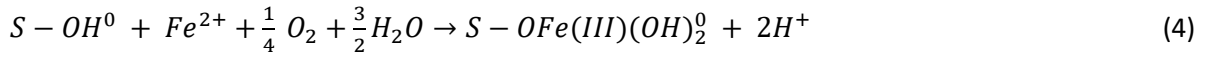
Resulting Rate Equation:

$$-\frac{d[Fe(II)]}{dt} = k_{het} \frac{[S-OH^0][Fe(II)][O_{2,(aq)}]}{[H^+]}$$ (5)

Where: $[S - OH^0]$ is the concentration of iron hydroxides (M)

$[Fe(II)]$ is the concentration of divalent iron (M)

$[O_{2,(aq)}]$ is the concentration of dissolved oxygen (M)

$[H^+]$ is the concentration of hydrogen ions in solution (M)

k_{het} is the rate constant of heterogeneous iron oxidation ($M^{-1} s^{-1}$)

From the above rate equation, it is evident that the rate at which iron is removed from the groundwater is proportional to the concentration of dissolved oxygen, and inversely proportional to the concentration of hydrogen ions in solution. Therefore, subsurface iron removal is facilitated by high dissolved oxygen concentrations and relatively high pH groundwater. The groundwater at 't Klooster is slightly basic (higher pH) in nature (see Appendix 1). This makes it a suitable location for subsurface iron removal by aeration.

2.3 Geologic and Hydrogeologic background

To explain and support any findings from the ERT data, it is necessary to first study the (hydro)geologic details of the subsurface that is under investigation.

The area around pumping station 't Klooster slopes down from the south-east to the north west. Overall, the groundwater flow follows this direction (Willemsen, 1998). The unconfined aquifer that 't Klooster taps into is quite shallow. For that reason, only the hydrogeology of first 50 meters of subsurface is studied in detail. These top 50 meters can be subdivided into three geologic formations: the Twente formation (0-6m), the Kreftenheye formation (6-18m) and the Oosterhout formation(20-50m).

The Twente formation is characterized by very fine to medium fine sands. The Kreftenheye formation is characterized by medium to very coarse sand, with a significant amount of gravels. The Oosterhout formation is characterized by very fine to very coarse sand, with local clay lenses (TNO-GDN, 2020).

They are all water bearing formations and can therefore all be grouped into one hydrogeological package. The hydrogeological base is theorized to be the Breda formation, found at a depth of approximately 65m and is characterized by fine sands and clayey sediments (Folmer et al., 2012). Other studies suggest the hydrogeological base to be shallower, at a depth of 30-35 meters and in the Oosterhout formation (Willemsen, 1998). The Oosterhout formation rapidly transitions to very fine sands. This impedes both horizontal and vertical groundwater flow, limiting prospects for deeper groundwater extraction (Folmer et al., 2012), and thus potentially forming the hydrogeological base. Analysis of ERT data can potentially identify the hydrogeological base. Figure 3 is a graphical

5

representation of a NW to SE cross-section. The location and depth of the well intakes at 't Klooster are denoted by a thick black vertical line.

In a recent study of geophysical well logs combined with ERT data (see Karaoulis et al., 2019), the upper 6m of the subsurface were identified as dry sand. This is followed by a sandy layer with significant heterogeneity (fine sand to pockets of boulders). , the upper 4 meters of this layer form the vadose zone, where pores are partially saturated. The majority of the sediment found at 't Klooster are braided river deposits. See Appendix 2 for an image of the interpretation of this study.
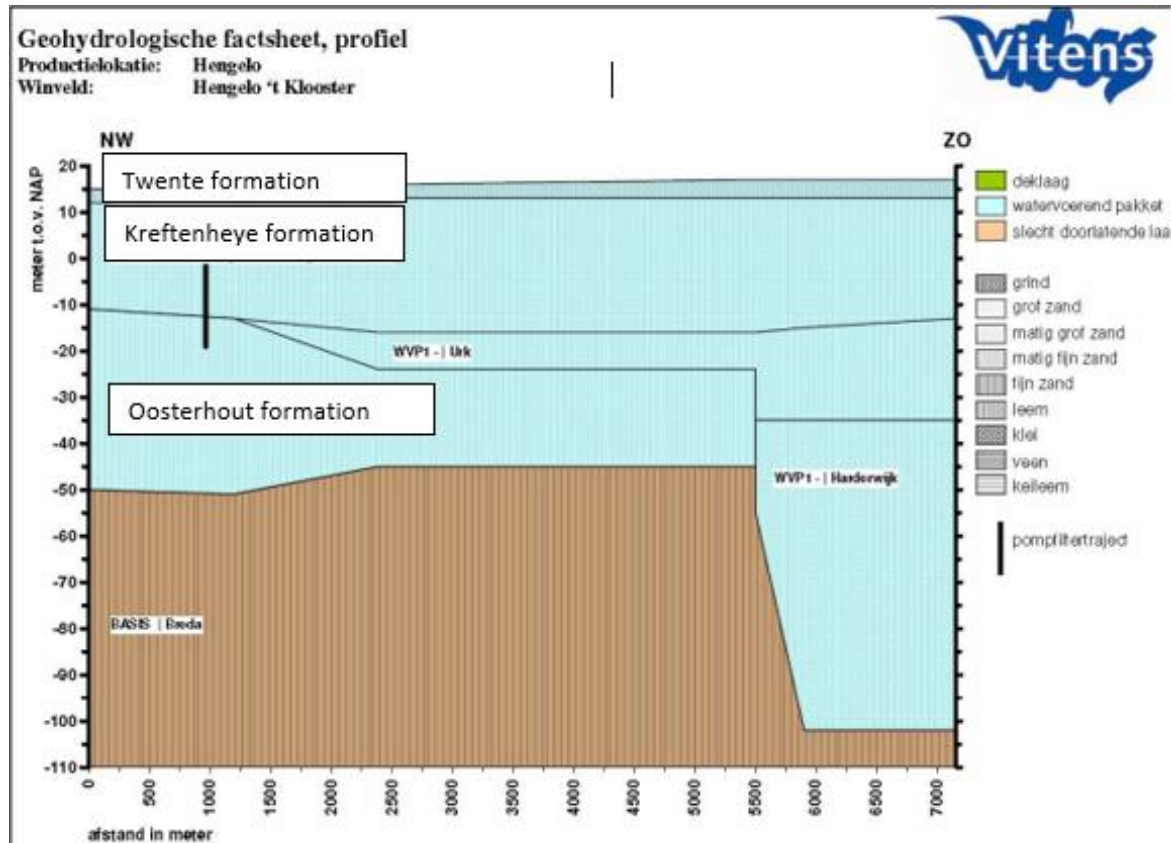
Figure 3: : NW-SE cross section of the project area. The well screen depth and approximate location of wells is denoted by the vertical black line. The Twente, Kreftenheye and Oosterhout formation make up the water bearing package. From: Folmer et al. (2012)

2.4 Time Lapse ERT
The data that is analyzed in this study is a set of time lapse ERT data which was collected at 't Klooster between the 14th of September 2018 and the 1st of October 2018.

2.4.1 Electrical Resistivity Tomography
Quadripole electrical resistivity tomography features a combination of 2 current electrodes (A,B) and 2 potential electrodes (M,N). To inject an electrical current I into the subsurface, the current electrode pair A (+I) and B (-I) are set up. The resulting electric potential difference between the potential electrodes is measured (Samouëlian et al., 2005). The potential difference in a homogeneous half space is expressed as follows:

$$\Delta U = \frac{\rho I}{2\pi}\left[\left(\frac{1}{r_{MA}} - \frac{1}{r_{NB}}\right) - \left(\frac{1}{r_{NA}} - \frac{1}{r_{MB}}\right)\right] \tag{6}$$

Where: ΔU is the potential difference (Volts)

ρ is the electrical resistivity (Ohm m)

I is electrical current (Amperes)

r_{ij} is the distance between potential electrode 'i' and current electrode 'j' (m)

Dropping the assumption of a homogeneous half space gives and rearranging equation 6 for what is now apparent resistivity ρ_a yields:

$$\rho_a = \frac{\Delta U}{I} 2\pi \left[\left(\frac{1}{r_{AM}} - \frac{1}{r_{BN}} \right) - \left(\frac{1}{r_{AN}} - \frac{1}{r_{BM}} \right) \right]^{-1} \tag{7}$$

Where $2\pi \left[\left(\frac{1}{r_{AM}} - \frac{1}{r_{BN}} \right) - \left(\frac{1}{r_{AN}} - \frac{1}{r_{BM}} \right) \right]^{-1}$ is dependent on the configuration of the 4 electrodes. It is commonly referred to as the geometrical factor, denoted K. By method of tomographic inversion, these apparent resistivities are converted to a model representing the true resistivity distribution of the subsurface.

2.4.2 Experimental Set Up

The set-up of the survey is shown in Figure 4. The wells in Figure 4 are 7 of the 12 groundwater extraction wells present at groundwater extraction field 't Klooster. The ERT study was carried out around pumping well 13-18, named well 13 for conciseness.

Figure 4: Image of well field 't Klooster. The red cross shows the location where time lapse ERT was performed. From: Karaoulis et al. (2019)

To facilitate the time-lapse cross-hole study, 4 boreholes were drilled: to the north, east, south and west of well 13. Figure 5 below shows the exact set-up of the 4 ERT boreholes, as well as the location of the distributed temperature sensing (DTS) measurements and extraction well 13.
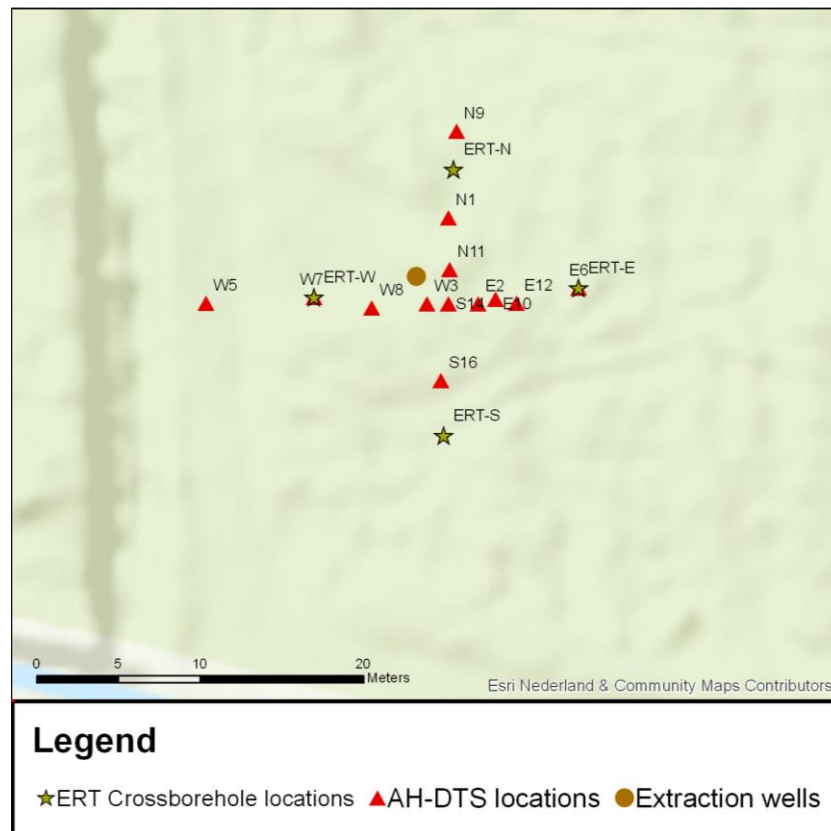
Figure 5: Zoomed in image detailing the location of the 4 boreholes for ERT, as well as the position of DTS measurements, and the location of groundwater extraction well 13.

Each of the 4 boreholes surrounding well 13 are roughly 40 meters deep and reinforced with PVC. They were all fitted with 48 electrodes. Of these 48 electrodes, 10 were positioned on the surface, and 38 down the borehole, each with a spacing of 1m, going down to a depth of 38m. The boreholes were not backfilled. LaBreque et al. (1996) showed that it is important to maintain a sufficiently small ratio of the separation of boreholes and the depth of placed electrodes. In order to avoid losses in resolution, this ratio should be limited to 0.5. The maximum distance between boreholes in this experiment is 15 meters, resulting in an aspect ratio of approximately 0.4. This is below the recommended value.

2.4.3 Survey Procedure

This section outlines the manner in which data was collected at 't Klooster in the Fall of 2018. The survey can be divided into two stages: the survey design stage and the monitoring stage. The data collection system used is the DAS-1 Electrical Impedance Tomography System. It is an 8-channel system capable of imaging the subsurface in 3D with ERT, with typical measurement precision of 0.05% (Multi-Phase Technologies, 2007). This is well below the 0.5% changes observed by Marios et al. (2019).

Design Stage

Geoelectric surveys, like the one carried out at 't Klooster are often limited by time and cost. It is thus generally impossible to test all possible electrode configurations in an ERT survey. It is therefore

interesting to only select optimal electrode arrangements that yield the highest resolution inverted model. With the onset of advanced multi-channel instruments, it has become possible to specify such desired electrode array configurations for specific survey types. Many selection algorithms exist, one of the most effective ones being Wilkinson's *Compare R* method (Loke et al., 2013). It aims to maximize the inverted model resolution whilst considering only a fraction of a total set of possible measurements (Wilkinson et al., 2011).

This method starts with a small base data set obtained from bipole-bipole measurements. The resolution matrix (R) of this data set is calculated. With each additional quadrupole array added to this dataset, the change in R is computed. The X arrays that result in the largest improvements of R and are sufficiently orthogonal (i.e. contributing new information), are then added to this base dataset (Loke et al., 2013). X is the desired number of arrays; and is determined prior to surveying.

The DAS-1 used at 't Klooster is an 8-channel system, meaning that every measuring instance is a combination of eight 4-electrode arrays. To speed up acquisition, the combined eight best 4-electrode arrays were added to the base dataset, rather than single 4-electrode arrays. Prior to actual monitoring, the *Compare R* method was used at 't Klooster to design a cost and time effective survey. The following electrode configurations were selected by the algorithm: the gradient, pole-tripole and bipole-bipole arrays. The first configuration was used for in-hole measurements, the latter 2 were used for CHERT. Another metric used to disqualify array configurations during this design stage was the deviation in resistances measured by reciprocal measurements.

Monitoring Stage
During monitoring, the time-optimized survey from the design stage was used. No more reciprocal measurements were taken, however, every measurement was carried out twice to get a measure of the standard deviation between different measurements.

2.4.4 Measurements
In-hole ERT measurements
In-hole ERT measurements were performed at each of the 4 boreholes. For in-hole ERT, all 4 electrodes are positioned in the same well. In effect, it functions similar to surface-ERT (Maurer et al., 2009). Data was collected by means of gradient array. The spacing between both the current electrodes A and B and potential electrodes M and N remains constant. The potential electrodes are shifted along the borehole axis. Measurements were repeated, but with varied spacing between both potential and current electrodes. The spacing between current electrodes in different repetitions was varied 5 times, from 8m to 40m with increments of 8m. The spacing between potential electrodes was respectively varied from 1m to 5m with increments of 1m. This was done to image resistivity variations further away from the borehole. This is schematized in Figure 7(a). For the interpretation of in-hole geoelectric measurements, the geometrical spreading function used assumes that resistivities are axially symmetric around the borehole. This assumption has the consequence that in-hole measurements cannot determine with certainty the location of localized resistivity anomalies. In the phreatic aquifer found at 't Klooster, this type of anomaly could result from pockets of boulders, as predicted by Karaoulis et al. (2019). For that reason, it is important that in-hole data is combined with CHERT data, effectively mitigating this azimuthal ambiguity (Maurer et al., 2009).

CHERT measurements
Cross-hole electrical resistivity tomography was carried out between all boreholes. Figure 6 shows a sketch of the borehole setup and the 6 different measurement planes.

Figure 6: Top view of 4 boreholes used for in-hole ERT and CHERT. Labelled north, south, east and west for their position with regards to Well 13. The CHERT planes are numbered 1-6 for later reference. The position of well 13 is also marked.

Figure 7(b) and 7(c) show the electrode configurations used for CHERT: tripole-pole and bipole-bipole arrays. Tripole-pole measurements feature current electrode A and both potential electrodes in one borehole, and current electrode B in another borehole. For every position of current electrode B, A-M-N are shifted down their respective borehole. As with in-hole, multiple measurements were taken. The distance between potential pair M-N and A were varied from 1m up to 3m with increments of 1m. The distance between potential electrodes M and N was varied between 1m and 2m.

Bipole-bipole measurements feature current electrode A and potential electrode M in one borehole, and current electrode B and potential electrode N in another borehole. All electrodes are shifted down their respective borehole. Again, multiple measurements were taken at every current electrode location, with varying offset between A-M and B-N. This was varied from 1m to 4m with increments of 1m.

Figure 7: (a), left: gradient array for in-hole measurements. Potential electrodes M and N are shifted down along the borehole axis. (b), center: cross-hole bipole-bipole array. Potential electrodes M and N are shifted down along respective borehole axes. (c), right: cross-hole pole-tripole array. Current electrode A and potential electrodes M and N are shifted down along the borehole axes.

2.5 Data

Two weeks' worth of time-lapse CHERT and in-hole data were collected and inverted prior to this study. There was also DTS data available. Prior to analysis, the results of both datasets is presented.

2.5.1 DTS

DTS data was periodically collected at 13 locations (see Figure 5) approximately along the east-west and north-south axes of the ERT survey area. This yielded a temperature reading every 0.5m, down to a depth of 37m. This is visualized in the depth-temperature sections shown in Figure 8. DTS locations w7 and w3 did not have data for the desired time period. Locations w8 and w5 did not have data for the time period after the time lapse geoelectric survey.
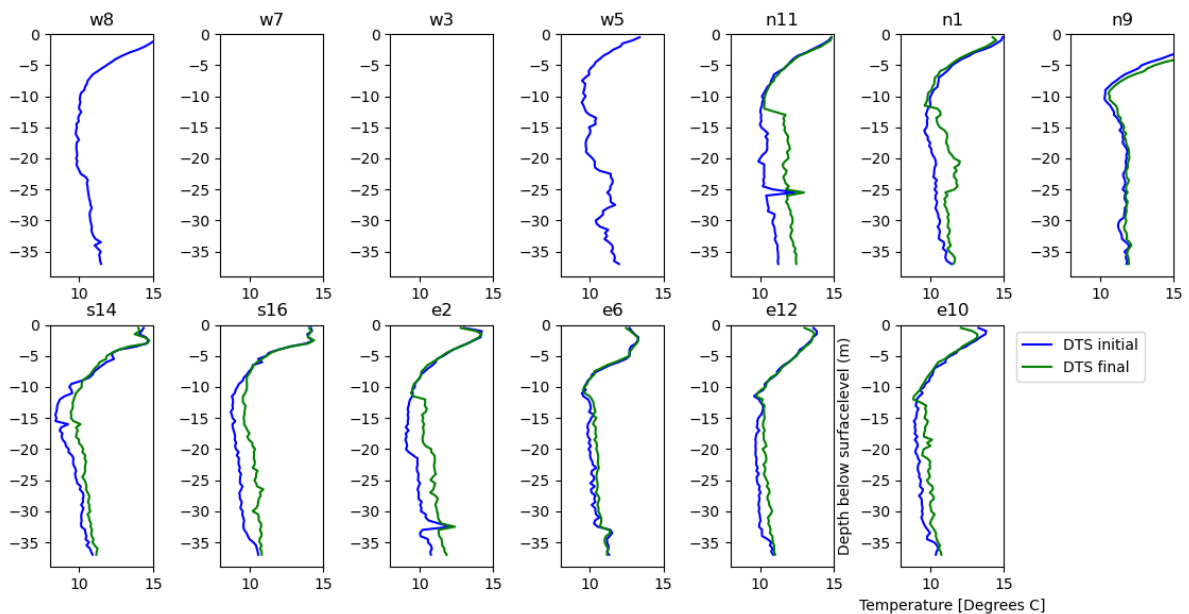
Figure 8: Temperature with depth plots of 13 DTS data locations. Blue lines represent data taken prior to the onset of the ERT survey. Green lines represent data take post ERT survey.

All locations show a general pattern of decreasing temperature for the first 10 to 15 meters below the subsurface. Beyond this depth, the temperatures gradually start increasing again. Also evident is that at depths beyond 10 meters, the temperatures recorded after the injection of the slightly warmer oxygenated water are consistently higher than those recorded prior. For shallower depths, this is not the case. This could outline the position of the saturated zone/water table.

2.5.2 ERT

Raw Data

2 weeks' worth of time lapse ERT data was collected. This was split into datasets with a time-step of approximately 1 hour between each, producing a 390 hour time-lapse dataset. Prior to inversion, it is important to look at the data quality. A possible metric of data quality are the galvanic contact resistances between the electrodes and the subsurface. The DAS-1 has an input impedance of 10^9 Ohms (Multi-Phase Technologies, 2007). To ignore the effect of the electrode contact resistance on measurements, the contact resistance should be 1000 times lower than the input impedance. For this reason, the DAS-1 features a maximum contact resistance 10^6 Ohms.

Contact resistances from the electrodes in the boreholes ranged from 536 Ohms to 18200 Ohms, well below the limit. However, even below this limit, high contact resistances can result in noisy data (Robert, 2012 , Zhou et al., 2019). The highest borehole contact resistances were consistently recorded for electrode arrays concentrated in the shallow subsurface. This was the case for both the in-hole and cross-hole ERT surveys. This owes largely to the fact that this is the un/semi-saturated sand layer. Data from the 10 electrodes on the surface was not considered for inversion due to the extreme contact resistances.

For 't Klooster data, each measurement was repeated twice. The resulting standard deviation is also recorded by the DAS-1. Much like the trend in the contact resistances, the largest standard deviations were associated with measurements by electrode arrays positioned in the upper portion of the subsurface. This was particularly so for the in-hole gradient arrays. The resolution in the shallow region might therefore be limited by noisy measurements.

Inversion Procedure

Measured resistance data is converted to resistivity by process of inversion. The manner in which data is inverted can significantly influence the reliability of the output model. It is therefore important to consider this process before doing any kind of data analysis and interpretation.

Continuous developments in the field of inverse theory have spawned a range of different data inversion procedures with the aim of improving model resolution and/or computational speed. For time-lapse data, some of the most prominent current methods of inversion are: independent inversion, difference inversion , 4D inversion, and 4D inversion with an active time and/or space component (4D-AT(S)C) (Karaoulis et al.,2013). They differ in their regularization schemes, and have situational benefits over one another. 4D-ATC for example allows for piecewise continuous resistivity changes in time. This is necessary when resistivity changes in time are rapid/sudden. Regularization serves two purposes: 1) suppression of inversion artifacts resulting from measurement errors and 2) suppression of noise to image real resistivity changes (Karaoulis et al., 2011,2013). The resistivity contrast between injected oxygen rich water and local groundwater is expected to be in the order of single or even tenths of a percent. A fitting inversion scheme is therefore important.

The inversion scheme used for 't Klooster data is 4D Active Time Constrained inversion. For the sake of brevity, this section expands on this scheme only. The 4D-ATC inversion scheme continues with the

4D inversion algorithm devised by Kim et al. (2009). The base 4D algorithm defines the subsurface and the survey data as space-time domain objects. The following explanation is from Kim et al. (2009).

Through sampling, a sparse "reference" 4D model and corresponding data vector can respectively be defined as

$$\widehat{X} = \begin{bmatrix} X_1 \\ \vdots \\ X_t \end{bmatrix} \text{ and } \widehat{D} = \begin{bmatrix} D_1 \\ \vdots \\ D_t \end{bmatrix} \tag{8}$$

Where t is number of time steps in a survey, and X_i and D_i are the reference model and data vector at time step *i*, respectively. A consequence of this time and space component shared by both the model and the data vector is that the objective function to be minimized through inversion can contain a regularization term in the time as well as in the space domain. The objective function (9) is shown below. For more on 4D-inversion of DC resistivity data, please refer to Kim et al. (2009).

$$\|e^T e\|^2 + \lambda \Psi + \alpha \Gamma \tag{9}$$

Where: e is the misfit vector of the data,

               Ψ is the value representing regularization in space

               Γ is the value representing regularization in time

               λ is the weight controlling regularization in space to the overall inversion

               α is the weight controlling regularization in time to the overall inversion

A limitation of having α be constant is that inappropriate smoothing in time may occur, suppressing actual variations resulting from water extracting or injection. The 4D scheme assumes changes from one-time step to another will be small. With relatively sudden processes such as the injection of warmer water, this assumption is not always appropriate. To have the time regularization factor allow for relatively rapid changes over time in an expected spatial region, 4D-ATC inversion replaces the constant α with diagonal matrix $\widehat{A}$ with dimensions $(n \times t) \times (n \times t)$. n is the number of parameters of a model in space, at each reference time t. This means that different degrees of time regularization can be performed at every point in the model space and time. In other words, time regularization is active. To fill in the values of $\widehat{A}$, it is necessary to identify the time steps during which the change in the model is significant. This is done by pre-estimating the resistivities at each time step before completing an iteration of 4D-ATC. The degree of change from one time step to another can then be quantified by looking at the ratio of resistivity at one time-step and its predecessor (Karaoulis et al., 2011). Regions where large resistivity variations are expected are then assigned small Lagrangian values, and vice versa for regions with little to no expected change. For more detail on 4D-ATC, please refer to Karaoulis et al. (2011). The inversion algorithm is implemented in inversion software Res3DInv.

Inverted Data

The output of the 4D-ATC inversion were 390 3D volumes with dimensions: 15mx15mx49m. Each volume consists of 11025 cells that were each assigned a resistivity value. Each cell has dimensions of approximately 1m x 1m x 1m. A visualization with Paraview is shown below in Figure 9:
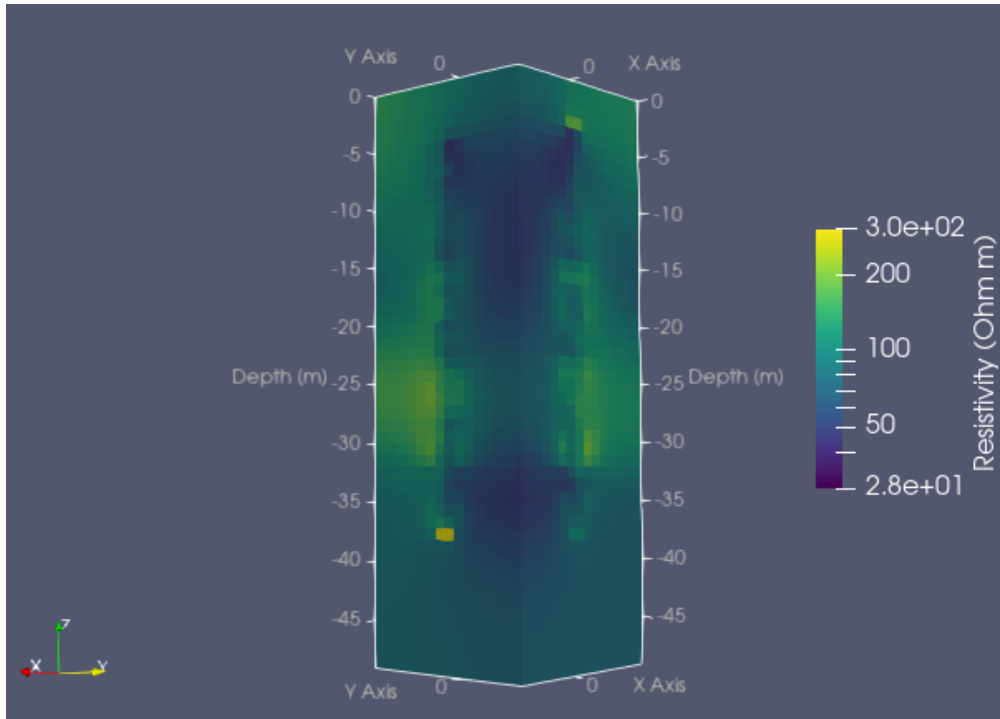
Figure 9: 3D representation of resistivity values at the onset of ERT monitoring: time t = 0 hours.

2.5.3 Well Data

A spreadsheet containing 't Klooster operating schedule was available. At intervals of 1 hour, this detailed when which well was active and whether it was extracting or injecting groundwater. For the purpose of this investigation, only the activity of wells 8, 9, 10 and 13 was considered. The other wells were deemed too far away to reliably detect their influence with ERT measurements. Additionally, this spreadsheet detailed the pump capacity of each well in m^3 per hour, as well as the depth of the well filter. The most important data are summarized in the data table below.

Table 1 showing the depth and pump capacity of the 4 wells of interest at 't Klooster. All well names are abbreviated to the first number in their name: 8, 9, 10 and 13 throughout this report.

Well	Depth of filter [m]	Pump Capacity [m³/hr]
Well 08-11	19,68 - 34,00	133
Well 09-12	20,19 - 29,50	133
Well 10-13	21,00 - 29,00	133
Well 13-18	17,81 - 32,00	133

3. Results and Analysis

Electrical resistivity depends on a variety of factors. Mineralogy, tortuosity, porosity, degree of saturation, temperature and the chemical composition of the pore fluid all play a role. In this study, we are interested in the (potential) resistivity changes caused by the operation of pumping wells, particularly when injecting slightly warmer, oxygen rich water. Any observed changes in resistivity in the saturated zone should therefore be driven by groundwater temperature changes, but also possibly water composition, as dissolved divalent iron is oxidized to trivalent iron. This trivalent iron is not a free ion. It precipitates out of solution (see Section 2), hereby taking away from the total ionic mobility. This is supported by a study showing that the reduction of trivalent iron to divalent iron results in

14

noticeable increases in electrical conductivity (Regberg et al., 2011). Despite this, Karaoulis et al. (2019) demonstrated that the injection of warmer (by 1-2 degrees Celsius) oxygenated water resulted in consistent reductions in resistivity. This suggests that the effect of iron precipitation on fluid electrical conductivity is smaller than the effect of temperature. This is possibly because other ions such as Mn^{2+} with similar charge and mobility to Fe^{2+} remain in solution, mitigating the effect of reduced Fe^{2+} concentrations. Compared to the effect of temperature, and potentially total dissolved solids, the effect of increased concentrations of dissolved oxygen in groundwater is negligible, and therefore not considered.

For the purpose of this study, changes in resistivity in the saturated zone are therefore primarily attributed to changes in temperature. This allows for the conversion of resistivity to temperature data by means of a model. The benefit of this is that temperature data can be additionally calibrated by measured DTS data.

3.1 Resistivity to temperature models

Temperature controls 2 properties that influence the electrical conductivity of a soil: 1) Fluid viscosity, which governs the mobility of charge carriers and 2) Grain surface ionic mobility (Hayley et al., 2007). An increase in temperature therefore results in increased charge carrier mobility, and increased grain surface ionic mobility. Correlating temperatures to resistivities requires a relationship between the two.

Van Ballaer (2020) evaluated the performance of several different models relating electrical resistivity to temperature. It was determined that the best performing models were Corwin and Lesh's (2005) corrected Sheets and Hendrickx's (1995) exponential model, Wraith & Or's (1999) polynomial model and Hermans et al.'s (2014) petrophysical model. Both the exponential and polynomial model are purely empirical. They therefore do not consider petrophysical relationships as in Hermans et al.'s (2014) model. Furthermore, they are based on fluid electrical conductivity tests, rather than on bulk conductivity, which is the property obtained by ERT. For that reason, Hermans et al.'s (2014) model is selected. Hermans et al.'s (2014) model is a combination of the empirically determined ratio model and Archie's law (1942). For the derivation, see Van Ballaer (2020).

Hermans et al.'s petrophysical model:

$$T_2 = \frac{\sigma_{b2}}{\sigma_{b1}}(T_1 - T_{ref}) + \frac{\frac{\sigma_{b2}}{\sigma_{b1}}-1}{m_{f,T_{ref}}} + T_{ref} \tag{10}$$

Where: T_i is the temperature at time i (°C)

σ_{bi} is the bulk electrical conductivity at time i (S m^{-1})

T_{ref} is the reference temperature (°C)

$m_{f,T_{ref}}$ is the fractional change in electrical conductivity at T_{ref} (°C^{-1})

Equation (8) suggests that temperature is inversely proportional to resistivity. The main assumptions that this model makes are: 1) Grain surface conductivity is negligible, 2) Pores are fully saturated, 3) the fractional change in electrical conductivity, $m_{f,T_{ref}}$ is constant, 4) precipitation/dissolution effects are negligible. The first assumption is valid in course grained soils such as the aquifer at 't Klooster, as grain surface conductivity increases with decreasing average particle size (Hermans et al., 2012). The

second assumption is only valid in the saturated zone. This equation is therefore not valid in the vadose zone (up to 10 meters). For the third assumption: m_f changes with temperatures. However, since the induced temperature increase is limited to just several degrees Celsius, this is a fair assumption. As outlined in the beginning of this section, the last assumption appears to be confirmed by results from Karaoulis et al. (2019). It could be confirmed by chemical modelling. For the conversion the 3D resistivity distribution to a 3D temperature distribution, T_1 is required for every cell with resistivity data. This is achieved by Universal Kriging 3D Interpolation of DTS temperature data. Naturally, this results in error/uncertainty at points further away from data, particularly because the DTS data is relative sparse. This takes away from the reliability of absolute temperature estimates. To work around this, one could look at changes in temperature.

3.2 ERT and DTS

Two resistivity datasets are converted to temperatures. The first dataset is at the beginning of ERT monitoring. The second dataset is 390 hours later, the last 62 hours of which is the injection of warmer water. T_1 is taken to be the temperatures recorded by DTS just prior to the start of ERT monitoring. It is assumed that the initial temperatures are constant throughout the volume being monitored. Figure 10 shows the positions of the data grid resulting from ERT.
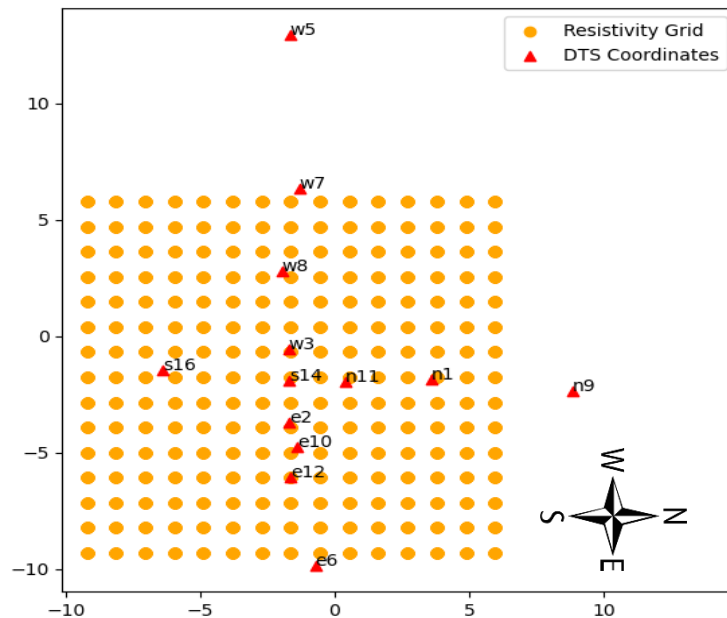
Figure 10: Top view of data grid created by Electrical Resistivity Tomography (orange) and the position of DTS measurements (red). W5 and N9 are outside of the region monitored by ERT.

The data corresponding to the 13 cells closest to the DTS locations are compared with respective DTS data in Figure 11. Resistivity estimated temperatures are generally similar to DTS measured temperatures. There are significant differences in the upper 10 meters. This can be explained by the fact that this is the dry and semi saturated zone, where Hermans et al.'s temperature conversion model no longer holds.
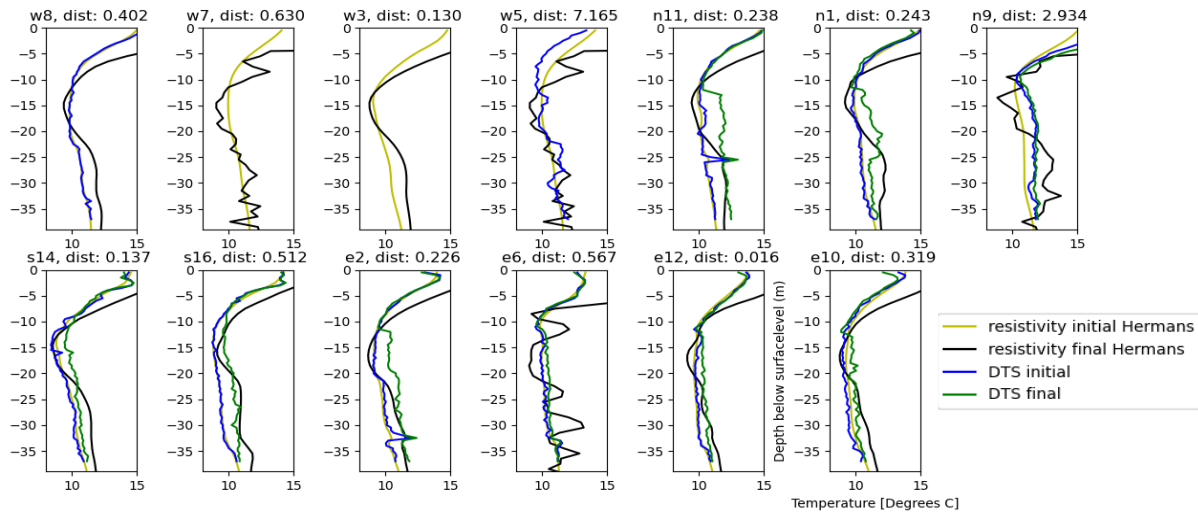
Figure 11: Plots of temperature with depth of DTS data and the nearest resistivity derived temperature data. 4 datasets are plotted, 2 (1 DTS, 1 ERT) from the beginning and two (1 DTS, 1 ERT) from the end of the ERT monitoring period. Each subplot is titled with the name of the DTS location, as well as the distance of the nearest resistivity derived temperature measurement (in meters).

For a more appropriate comparison, the data from the dry and semi-saturated zone (upper 10m) was thus discarded. To look at how the DTS and ERT estimated temperatures changed over the course of 2 weeks, the ratios of the final temperature to initial temperature were plotted. The titles of the subplots in Figure 11 show the distance between the DTS location and the nearest ERT derived temperature. It was decided that distances exceeding 0.5 meters could not be reliably compared. Figure 12 shows the resulting data.

The DTS data was smoothed using a Savitzky-Golay filter. This filter is commonly used to reduce high frequency noise (Gallagher, 2020), as is often observed in DTS data. For the raw DTS data, see Appendix 3. At DTS locations n1, n11, s14, and e2, the ratio in temperature change measured by DTS and estimated by ERT data agrees well, with Pearson correlation coefficients between 0.65 and 0.98. Further to the east of the volume constrained by ERT measurements however, the two ratios deviate. There are general patterns that seem to hold for all sections: Slight negative to no change in temperature from roughly -10 to -15m, more pronounced temperature increases recorded between -20m and -30m, and finally a drop in the magnitude of change in the deeper parts of the aquifer.
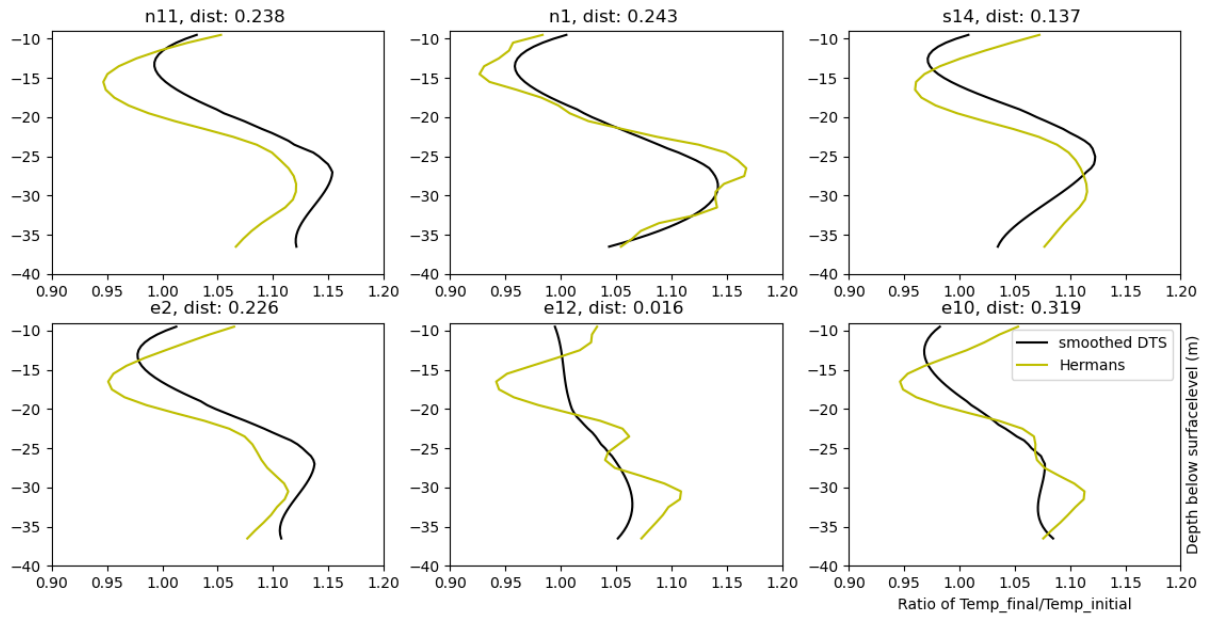
Figure 12: Plots of the ratio of the temperature after 2 weeks of ERT monitoring, and temperature at the onset of ERT monitoring. The distance between the DTS location and the nearest ERT temperature datapoint is denoted in the title of the subplots.

3.3 Depth Discretization

Visualizing the time lapse 3D volumes in Paraview showed that there were depth regions that experienced varying degrees and polarities of resistivity changes with time. This could say something about flow in these regions. In order to identify and approximately constrain these 'regions of interest', the time lapse data at the midpoint of the 15 by 15 cell grid created by ERT (Figure 10) was analyzed at different depths. The assumption here is that the volume is laterally homogeneous. From Figure 9 and Appendix 2, it is clear that this isn't consistently true. For the purpose of roughly identifying depth regions however, this is a fair assumption. The midpoint was chosen because it lies on the intersection of CHERT imaging planes 1 and 2 (Figure 6),and enjoys data contributions from all of the different CHERT planes shown in Figure 6. In other words, the CHERT sensitivity is expected to be high here. Furthermore, it lies at the intersection of the DTS temperature measurements, meaning T_1 has a relatively low associated error from earlier interpolation. Figure 13 shows the variance associated with the 3D temperature distribution interpolated from the sparse DTS data. At depths exceeding the DTS readings, it is significant, as well as away from the cross-pattern formed by the DTS measurements.
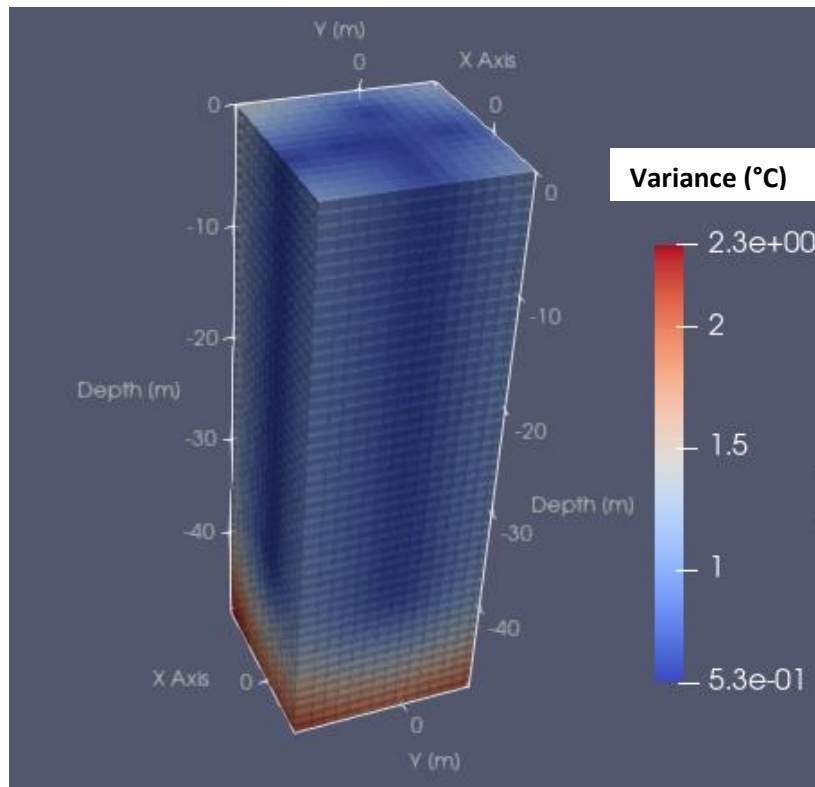
Figure 13: 3D variance distribution of interpolated temperatures from DTS data.

Single dimensional depth analysis is done for the first 48 hours of ERT surveying. During this period, pumping wells 8, 9 and 13 at 't Klooster were intermittently off and extracting water. If there are indeed distinct depth regions, this could stimulate differential resistivity changes at different depths. Since this depth range includes the vadose zone, Hermans et al.'s (2014) temperature model does not hold, and therefore measured resistivities are plotted rather than temperatures. For deeper regions, converted temperatures are plotted, rather than resistivities. ERT data was linked with the pumping schedule at 't Klooster. In this way, one can investigate which well 'action' is responsible for a change in resistivity.

3.3.1 Depth Region 1: 0m – 12.5m

Figure 14 shows the first 14.5 meters. Down to a depth of approximately 12.5 meters below the surface, resistivities increase with the extraction of water, and decrease again when no wells are operating. The decrease in resistivity is more rapid than the increase. It appears that the rate of decrease slows down if no wells are operating for long enough, as seen in the early morning of the 16th of September. The shallower the depth, the larger the magnitude of the changes. Beyond 12.5 meters depth, the trend is broken. This package is labelled the first 'depth region'. 14.5 meters is the start of the next depth section. Between 12.5 and 14.5 meters is a transition zone. The
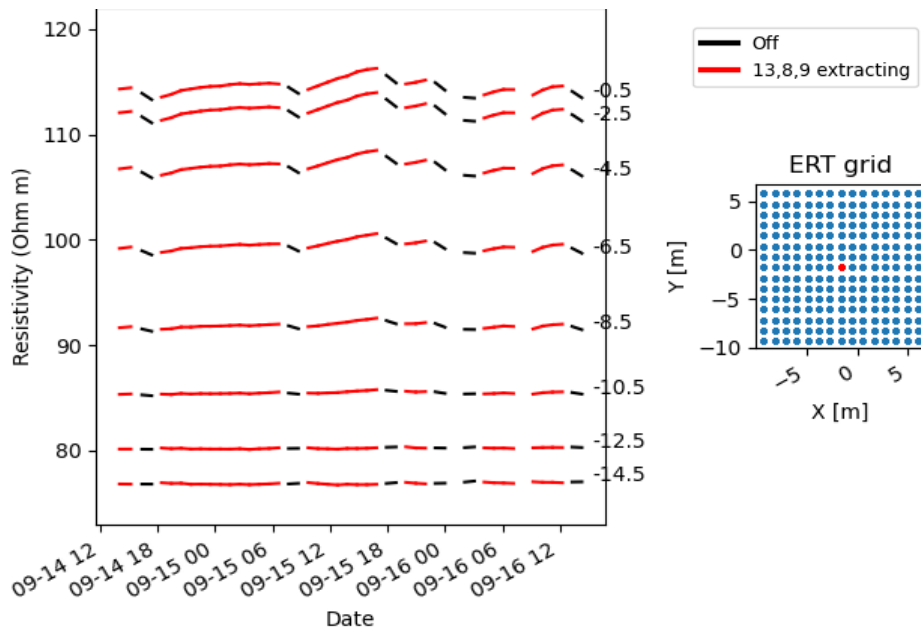
Figure 14: Resistivities at the mid-point of the ERT grid at depths between 0m and 12.5m. The orange dot in the grid on the right denotes the lateral position of the chosen point. Red lines denote wells 8, 9 and 13 extracting water at a rate of 133m³ per hour. Black represents no wells operating.

3.3.2 Depth Region 2: 14.5m – 34.5m

Figure 15 shows the ERT derived temperatures with depth at the chosen midpoint for depths between 14.5 and 36.5 meters. It is important to note that the absolute temperature values have significant uncertainty, as it relies on assumptions and interpolation using sparse data. This has likely resulted in some offset. More interesting is to look at the behavior of / changes in temperature, as this is more representative of the effects of well activity.
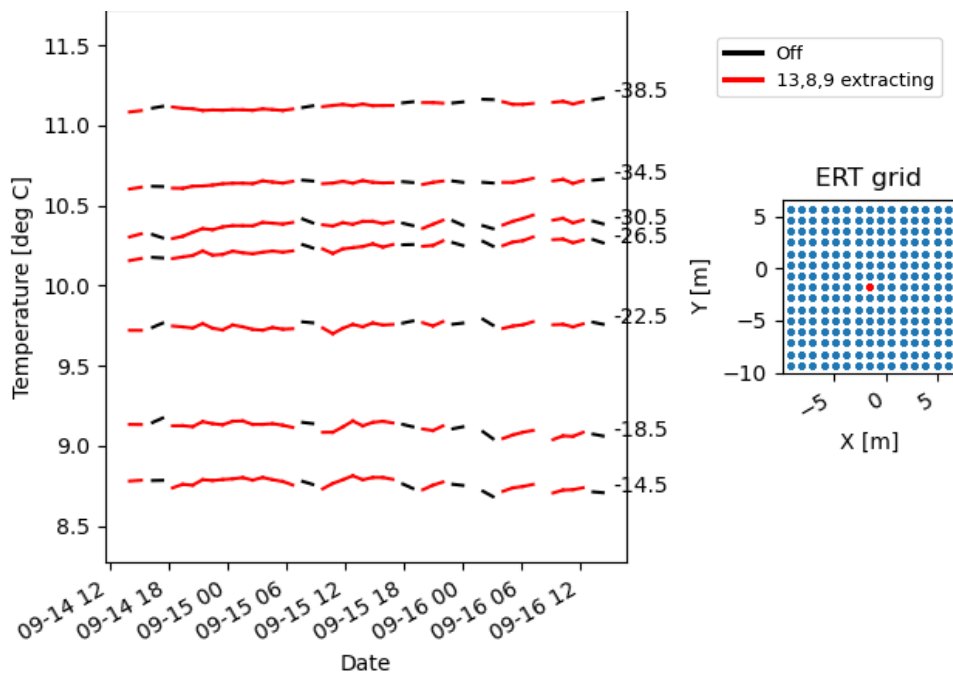
Figure 15: ERT derived Temperatures at the mid-point of the ERT grid at depths between 14.5m and 38.5m. The orange dot in the grid on the right denotes the lateral position of the chosen point. Red lines denote wells 8, 9 and 13 extracting water at a rate of 133m³ per hour. Black represents no wells operating.

The pattern is tougher to spot here. In general, temperatures increase when wells 8, 9 and 13 are extracting, and drop when the wells are off. The pattern breaks at around 34.5 meters below the surface. As temperature and resistivity are inversely proportional, this trend is opposite to that seen in the first depth zone. Upon closer inspection, there might be another separation between 22.5 meters depth and 26.5 meters depth. To confirm this, a 3D visualization is analyzed later in Section 3.3.4.

3.3.3 Depth Region 3: 34.5m – 48.5m
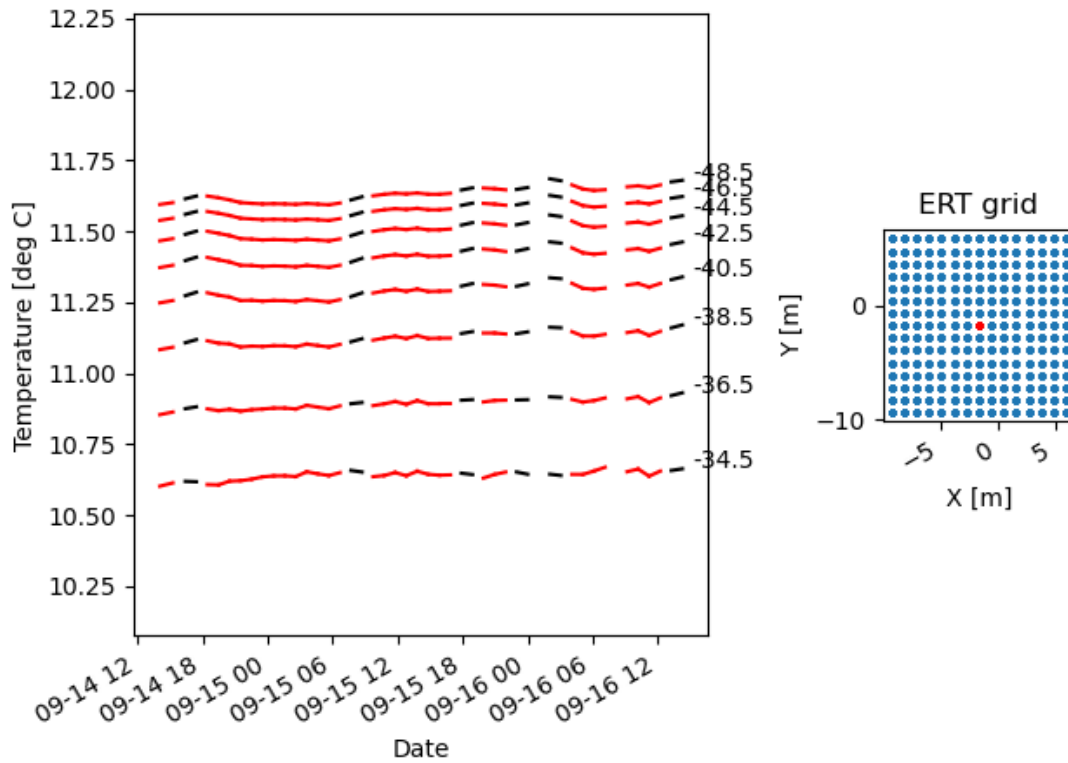
Figure 16: ERT derived Temperatures at the mid-point of the ERT grid at depths between 34.5m and 48.5m. The orange dot in the grid on the right denotes the lateral position of the chosen point. Red lines denote wells 8, 9 and 13 extracting water at a rate of 133m³ per hour. Black represents no wells operating.

Beyond 34.5 meters, the third depth region can be defined. This is shown in Figure 16. The general trend here is that when wells 8, 9 and 13 are running, temperatures drop. When the wells are off, the temperatures recover again. This is again opposite to effects seen in the previous depth region. The changes are more significant in the beginning of well activity, and gradually decrease. Note the temperature scale of the plots: changes in this depth zone are significantly smaller than in the previous depth zone, however, they are consistent. This suggests that the noise is not responsible for the patterns.

3.3.4 Visualization

From the 1-D plots, 3 depth regions responding differently to wells 8, 9 and 13 operating are identified. To see if these patterns held in 3D, 2 orthogonal 2D depth sections along CHERT planes 1 and 2 are visualized. To also include the effect of injecting warmer water, changes over the entire 390 hours of ERT monitoring were plotted. Figure 17 plots the change in resistivity at each depth along the east-west (1) and north-south (2) CHERT planes. The % change in resistivity is determined according to the following formula:

$$\left(\frac{\rho_i}{\rho_1} - 1\right) \times 100\% \tag{9}$$

With ρ_i being the resistivity at time t_i.

Both images confirm the existence of the 3 depth regions, as well as an additional 4th depth region between 22 and 35 meters below surface level.
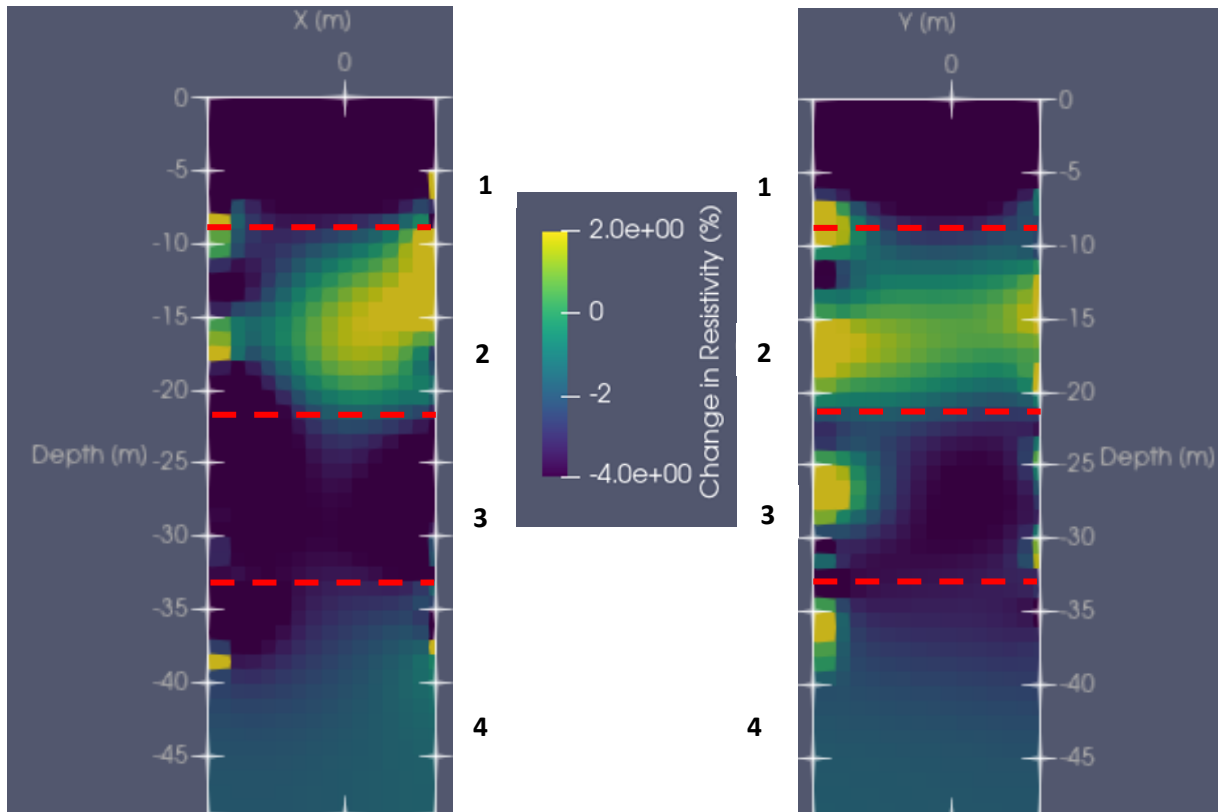
Figure 17: (a), left: CHERT imaging plane 2 plotting changes in temperature with depth. (b), right: CHERT imaging plane 1 plotting changes in temperature with depth. The changes are over a time period of 390 hours. 4 distinct depth regions can be identified, as was implied by the 1D analysis. These are labelled 1-4 and are separated by red lines.

To verify that the temperature conversion model accurately reflects these measured resistivity changes, the converted temperature change for the same CHERT planes and for the same 390 hours is shown in Figure 18. Again, the different response over time of the same depth regions is highlighted.
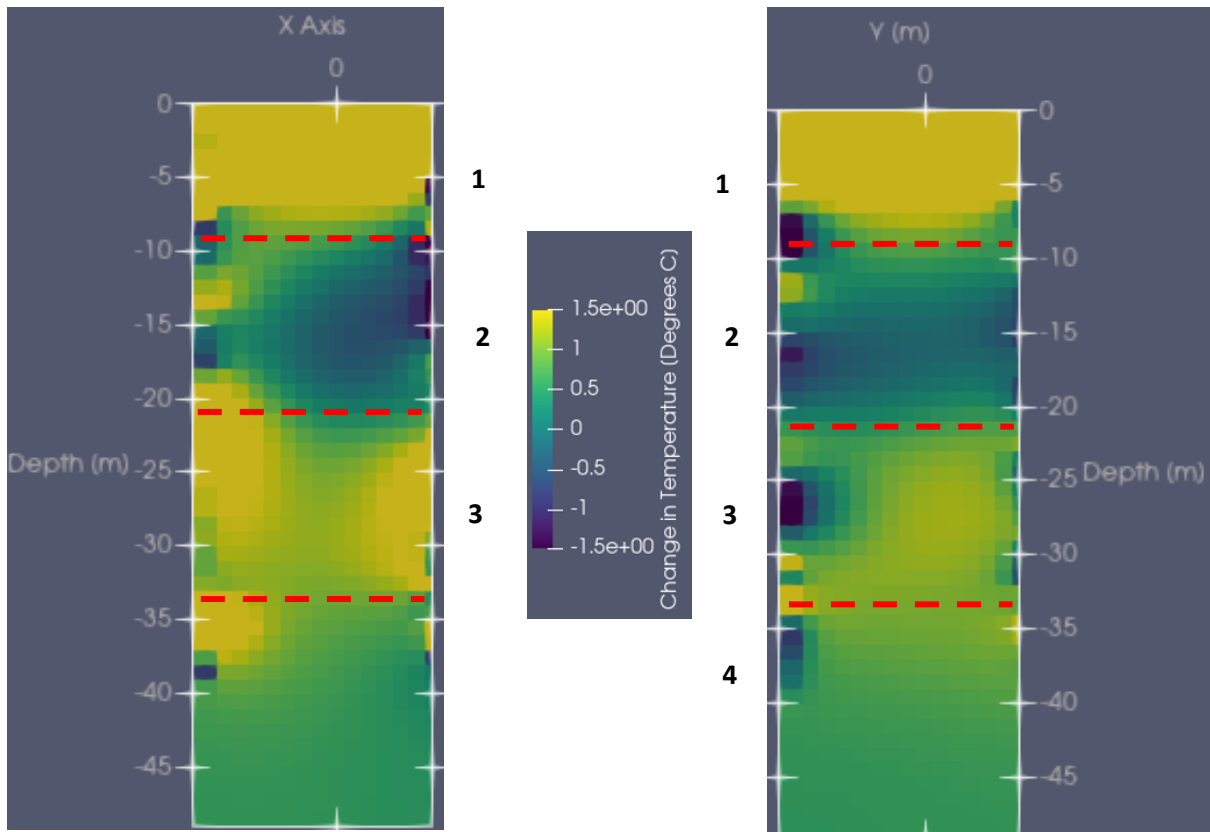
Figure 18: (a), left: CHERT imaging plane 2 plotting changes in temperature with depth. (b), right: CHERT imaging plane 1 plotting changes in temperature with depth. The changes are over a time period of 390 hours. 4 distinct depth regions can be identified, as was implied by the 1D analysis. These are labelled 1-4 and are separated by red lines.

Having effectively discretized the imaged volume into 4 regions of interest, it is now possible to analyze the horizontal changes at each depth region when different combinations of pumping wells are operating. The goal is to identify flow paths. To do this, a depth from each region is chosen: -6.5 meters, -17.5m, -28.5m and -36.5m. These depths are assumed to be representative of their corresponding depth region.

3.4 2D Horizontal Slices

The different combinations of wells operating are listed in table 2 for clarity:

Table 2 showing different well combinations operating during the 390 hour ERT survey and the different possible statuses of each well over this time period.

Well combinations	Well Action
8, 9, 13	Extracting / OFF
8, 10, 13	Extracting / OFF
8, 9, 10	Extracting / OFF
8, 10	Extracting/ OFF
13	Injecting

For consistency, the images this section plot estimated temperature change, rather than resistivity change. As with the DTS-ERT comparison in Section 3.2, the depth region corresponding to the dry and vadose zone is not considered in the estimated temperature comparison. Due to saturation changes, Hermans et al.'s (2014) model cannot be used to determine temperature changes.

Furthermore, due to shallow depth and high vertical permeability, the effect of rain and day/night temperature variations is significant here. This complicates isolating the temperature changes that result from well action. It can however provide insight on the effect of far away wells operating. For that reason, the resistivity changes at -6.5m are included in Appendix 4.

The longest time interval that is shared by all different combinations of wells that operated during the ERT monitoring period is 7 hours. For a fair comparison, all changes are therefore considered over a period of 7 hours. These 7 hours are always the first 7 hours just after a change in well action occurs (Eg: wells 8, 9 and 13 go from extracting to off). The manner in which temperature changes are calculated is as follows:

1. The temperature dataset at t_{i-7} is subtracted from the temperature dataset at t_i where i is the chosen times at which to evaluate temperature change. This gives the apparent temperature change ΔT_i. It is the absolute temperature change from t_{i-7} to t_i. . In equation form:
$$\Delta T_i = T_i - T_{i-7} \tag{10}$$

3.4.1 Wells 8, 9 and 13 extracting vs Off
Depth Region 2: 17.5 meters
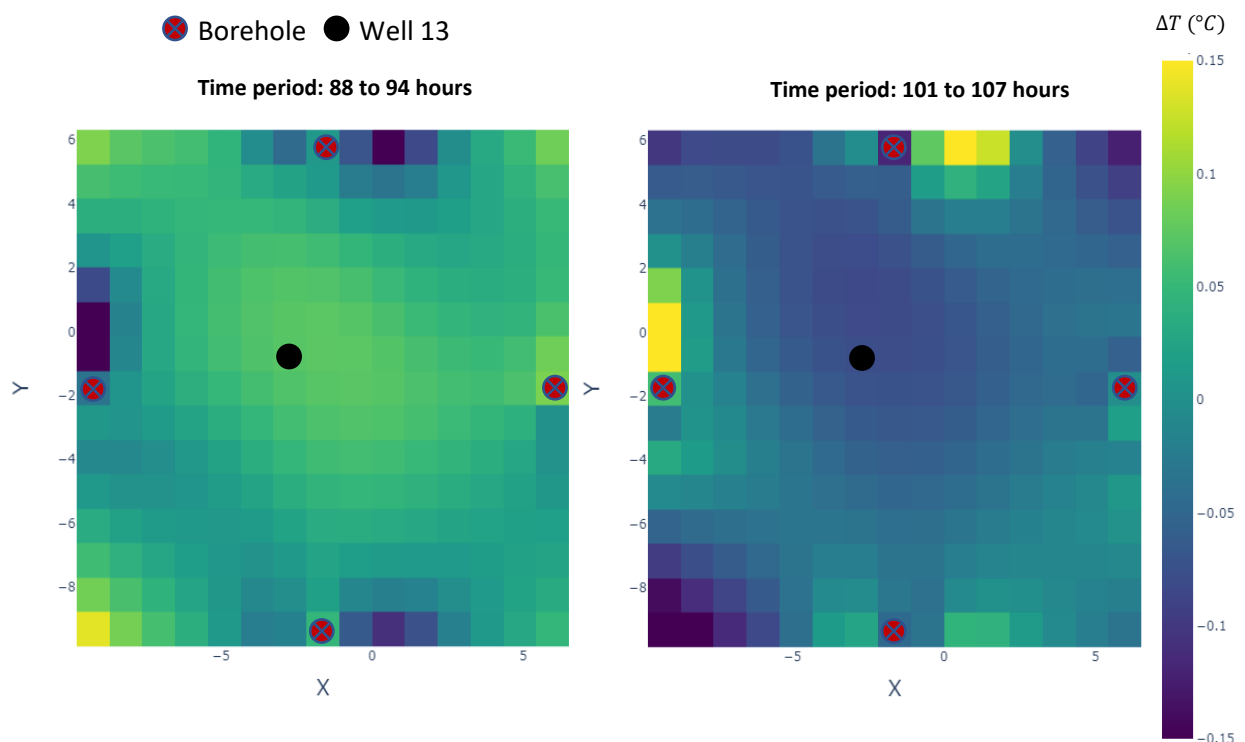
Figure 19: (a), left: Temperature changes at depth 17.5m after 7 hours of wells 8, 9 and 13 extracting. (b), right: Temperature changes at depth 17.5m after 7 hours of well inactivity.

Figure 19(a) shows the lateral temperature change that is estimated at a depth of 17.5m when wells 8, 9 and 13 extract ground water for 7 hours, at a rate of 133m³ per hour. Figure 19(b) shows the temperature changes for the first 7 hours after the wells are switched off. The approximate position of the boreholes, and pumping well 13 is marked. At and adjacent to the ERT boreholes, extreme temperature changes are estimated with the temperature conversion model. These are present at all depth regions, and in the same location. This could be a result of inversion or an effect of the open borehole. Disregarding these, the majority of temperature change happens in the vicinity of well 13.

24

When wells 8, 9 and 13 are extracting, a general temperature increase peaking at around 0.1 degrees Celsius is visible. A similar but opposite trend is seen when the wells are shut off for an equal time period. Changes extend from the center to the south-west corner of the visualized area. This is in the same direction as local groundwater flow.

To confirm that these changes are the result of the wells operating, a separate instance of wells 8, 9 and 13 operating for 7 hours and shut off for 7 hours is investigated in Figure 20. The ERT boreholes and well 13 are no longer marked, but remain in the same position for all of the 2D slices.
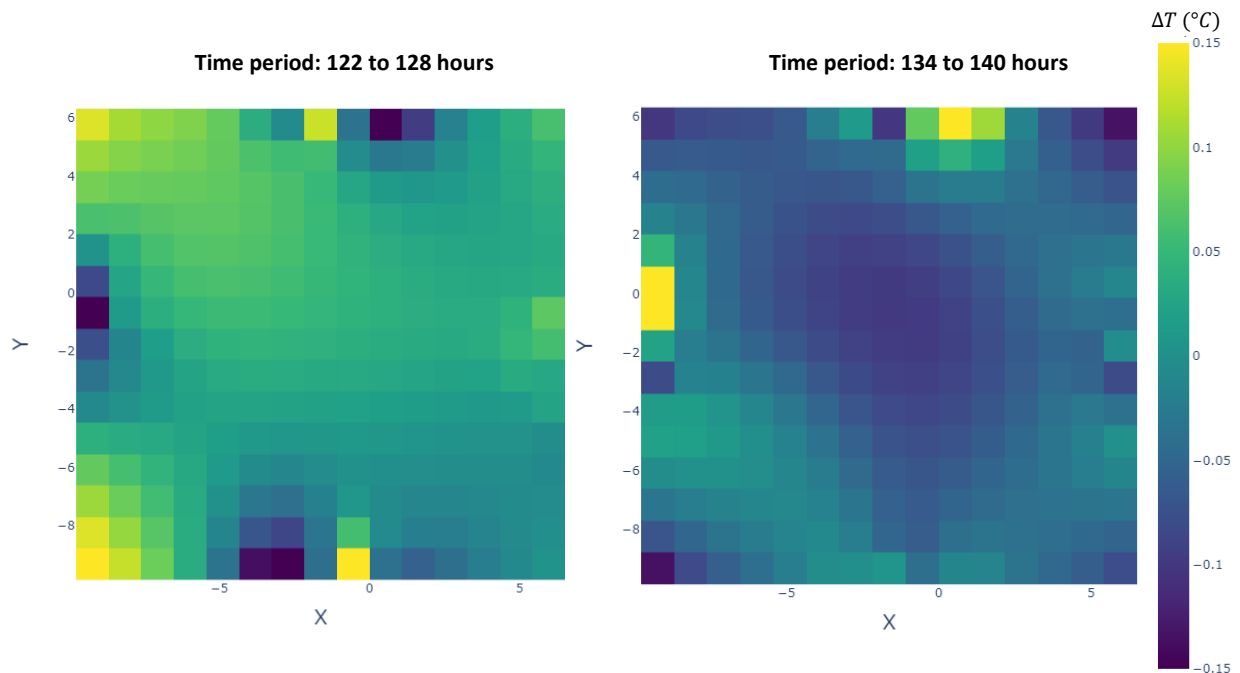
Figure 20: (a), left: Temperature changes at depth 17.5m after 7 hours of wells 8, 9 and 13 extracting. (b), right: Temperature changes at depth 17.5m after 7 hours of well inactivity.

The same patterns as in Figure 19 are visible: a general increase in temperature with groundwater extraction at wells 8, 9 and 13 and a temperature drop when the wells are switched off. Again change is concentrated around the position of well 13. This time, the increase in temperature is concentrated more towards the south-west of the section. Figure 20(b) shows that the drop in temperature over 7 hours of inactivity is still predominantly around well 13. This comparison of different 7 hour periods with the same well activity was done for all depth regions, with similar results. The changes are therefore consistent, confirming that the geoelectric survey seems adequate to image changes resulting from wells 8, 9 and 13 extracting ground water.

Depth Region 3: 28.5 meters
The next chosen depth was 28.5m. Figures 21(a) and 21(b) show the temperature changes after 7 hours of wells 8, 9 and 13 extracting water and inactive respectively. The chosen time period is the same as that in Figure 19. Like at a depth of 17.5 meters below surface level, the effect of wells 8, 9 and 13 extracting groundwater induces a minor increase in temperature (corresponding to a minor drop in resistivity). The opposite is once again observed in Figure 21(b). The distribution of temperature change is different than at 17.5 meters. The majority of temperature increase is in the

west and south-west of the section. The estimated drop in temperature with the wells off is similar to that observed at 17.5m depth , and is concentrated around well 13.
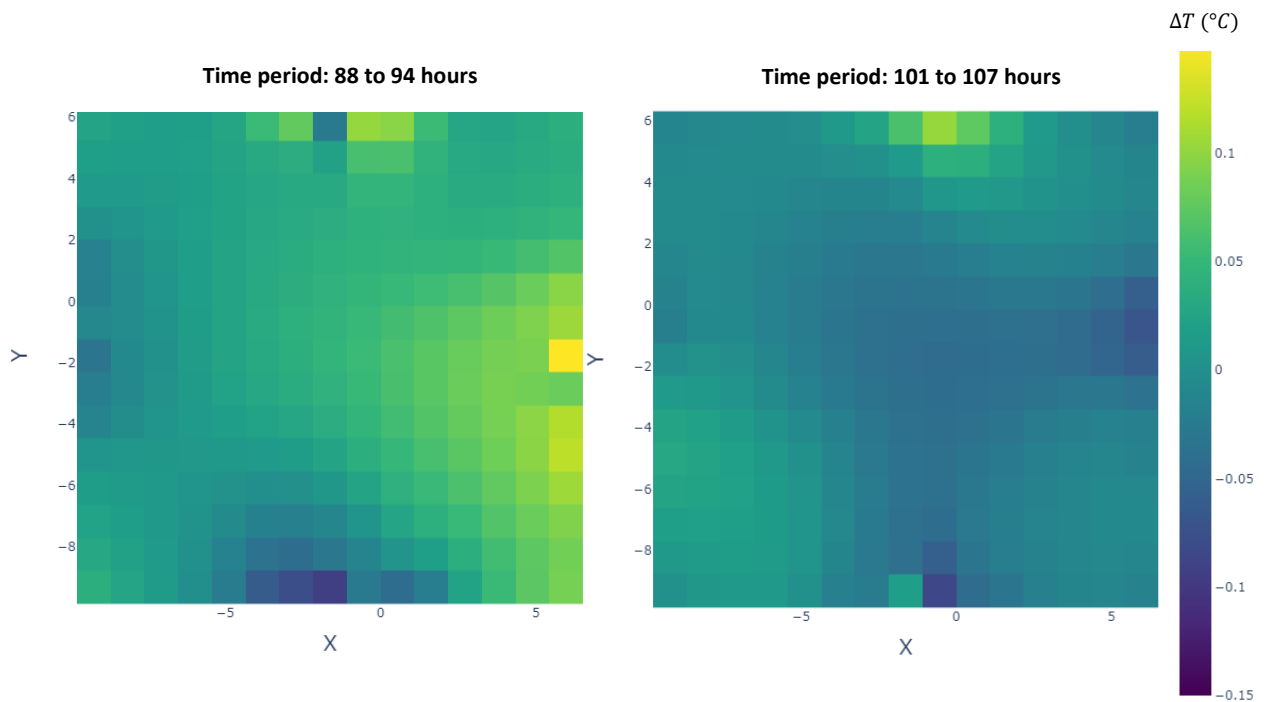
Figure 21: (a), left: Temperature changes at depth 28.5m after 7 hours of wells 8, 9 and 13 extracting. (b), right: Temperature changes at depth 28.5m after 7 hours of well inactivity.

Depth Region 4: 36.5 meters
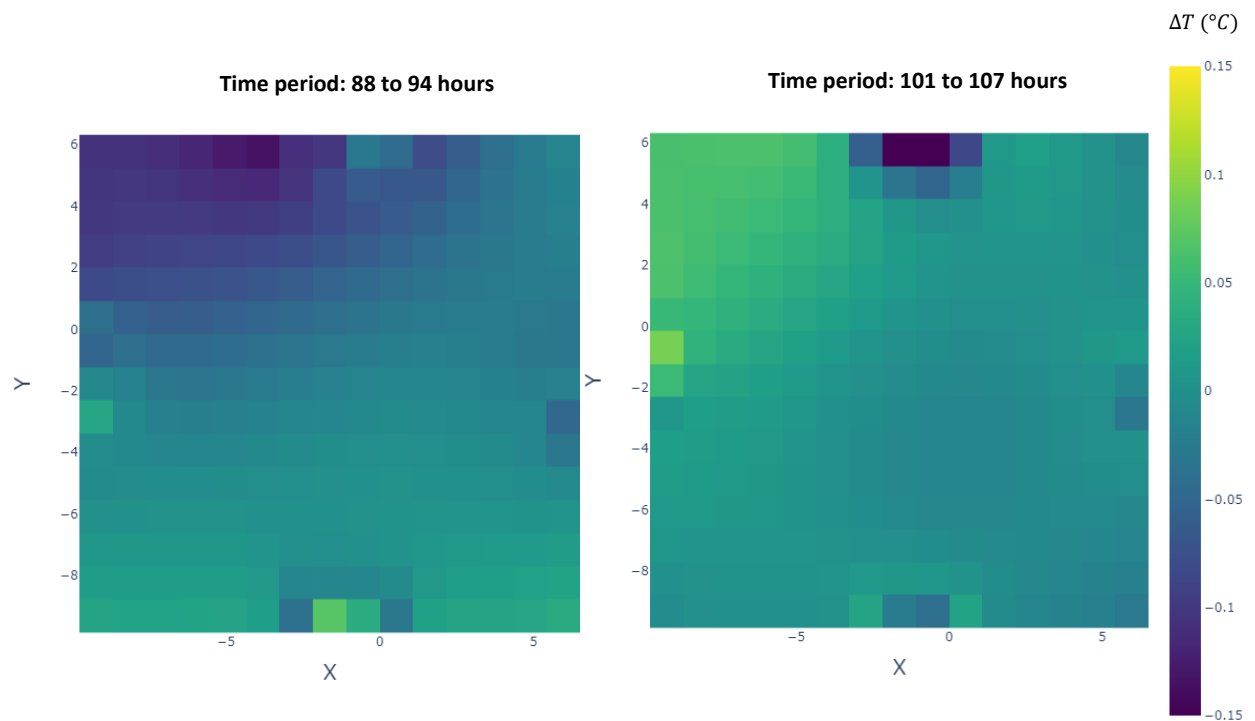
Figure 22: (a), left: Temperature changes at depth 36.5m after 7 hours of wells 8, 9 and 13 extracting. (b), right: Temperature changes at depth 36.5m after 7 hours of well inactivity.

26

Finally, depth region 4 is considered, by plotting a 2D slice at 36.5 meters below the surface – see Figure 22 above. Temperatures appear to decrease during groundwater extraction of wells 8, 9 and 13. When the wells are off a temperature increase is observed. This change is concentrated in the south-west corner of the section. Beyond this corner, the changes observed at 36.5 meters depth are noticeably smaller in magnitude than those observed at shallower depths.

3.4.2 Different Wells Extracting

So far, only the effect of wells 8, 9 and 13 extracting groundwater in unison has been investigated. Given the proximity of well 13 to the ERT setup, it most likely plays a role in the observed changes in resistivity/temperature. One of the goals of this thesis is to study the effect of wells further removed from the ERT setup. These are: wells 8, 9 and 10. To do this, this section looks at the effect of different well combinations.
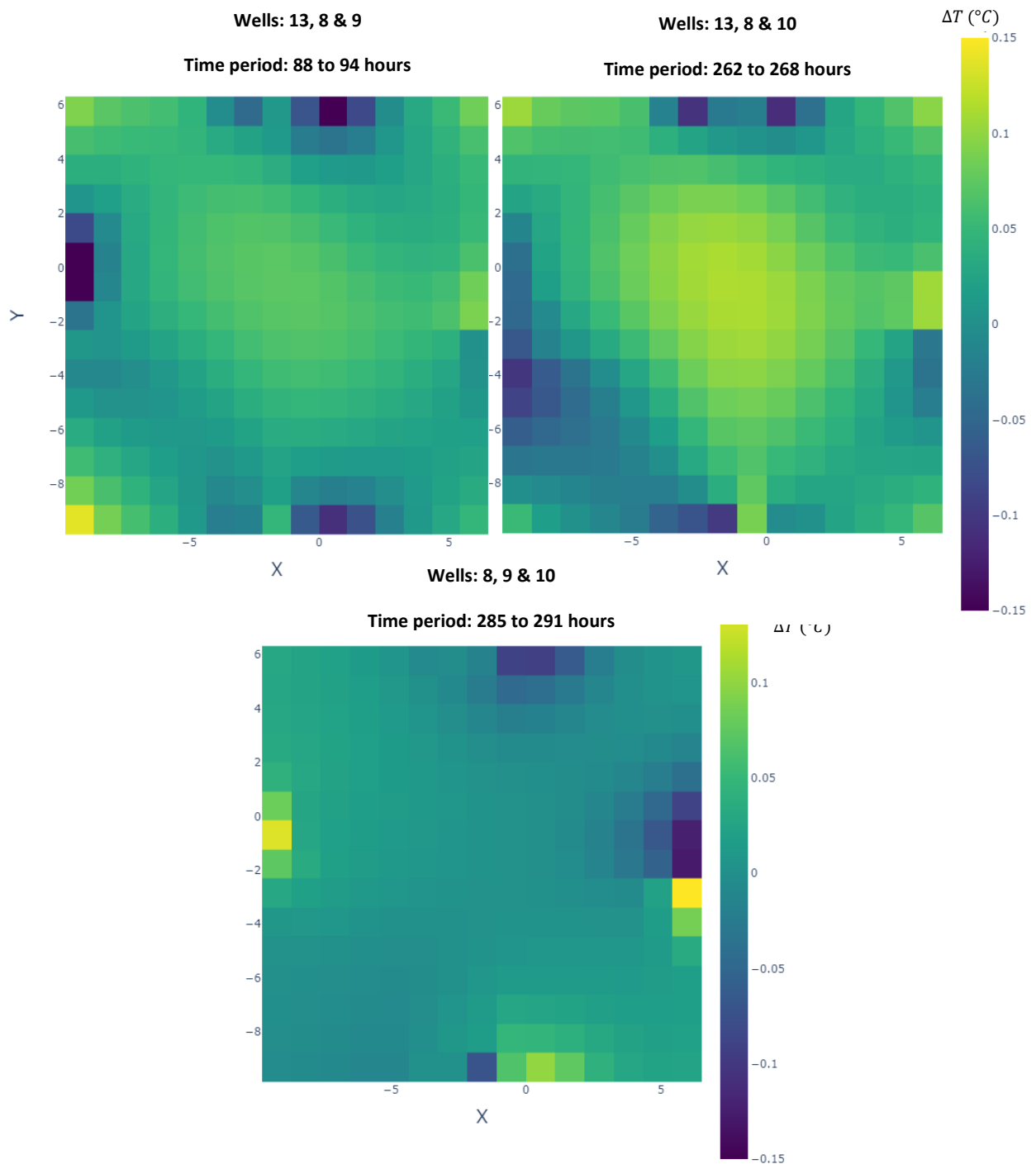
Figure 23: (a), up left: Temperature changes at depth 17.5m after 7 hours of wells 8, 9 and 13 extracting. (b), up right: Temperature changes at depth 17.5m after 7 hours of wells 8, 10 and 13 extracting. (c), bottom: Temperature changes at depth 17.5m after 7 hours of wells 8, 9 and 10 extracting.

At 17.5 meters depth, the temperature patterns seen in Figure 23(a) and 23(b) are very similar. Both estimate temperature increases around well 13. Rather than a circle around the position of well 13, changes are stretched along the diagonal of the slice from the north-east to the south-west. The temperature change is larger however when well 10 is extracting instead of well 9. When well 13 is inactive, and three faraway wells 8, 9 and 10 are extracting, there is no discernable change in temperature recorded. The anomalies surrounding the 4 ERT boreholes are seen at all depths.

28
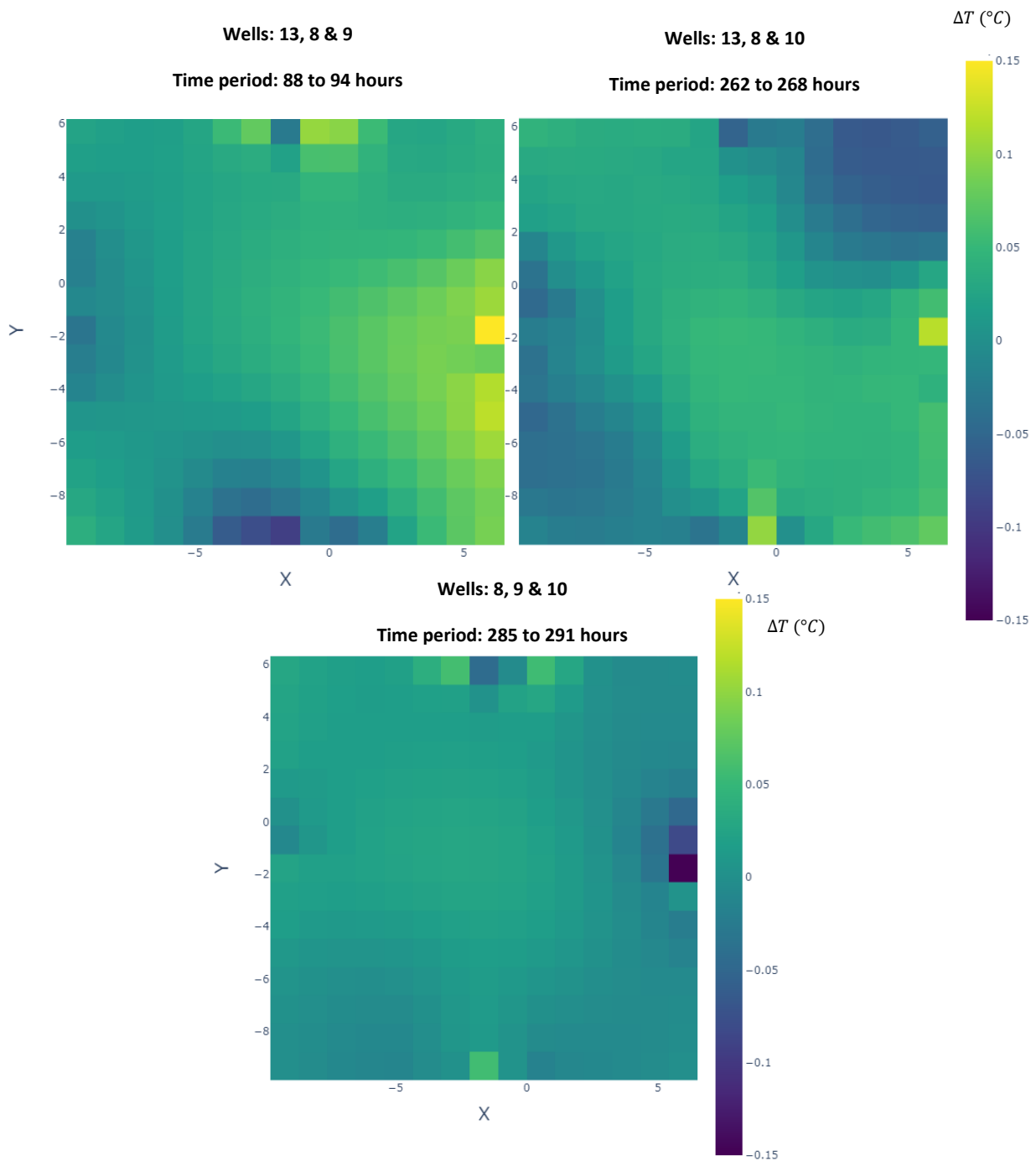
Figure 24: (a), up left: Temperature changes at depth 28.5m after 7 hours of wells 8, 9 and 13 extracting. (b), up right: Temperature changes at depth 28.5m after 7 hours of wells 13, 8 and 10 extracting. (c), bottom: Temperature changes at depth 28.5m after 7 hours of wells 8, 9 and 10 extracting.

At 28.5m depth, the difference between wells 8, 9 and 13 (Figure 24(a)) and 8, 10 and 13 (Figure 24(b)) extracting groundwater becomes more apparent. When, in unison with well 8 and 13, well 10 is extracting instead of well 9, a considerable drop in temperature is observed in the south-west and north-east corners of the section. A slight increase in temperature is still observed close to the well 13 for both. Once again, no discernable change is observed when well 13 is inactive.
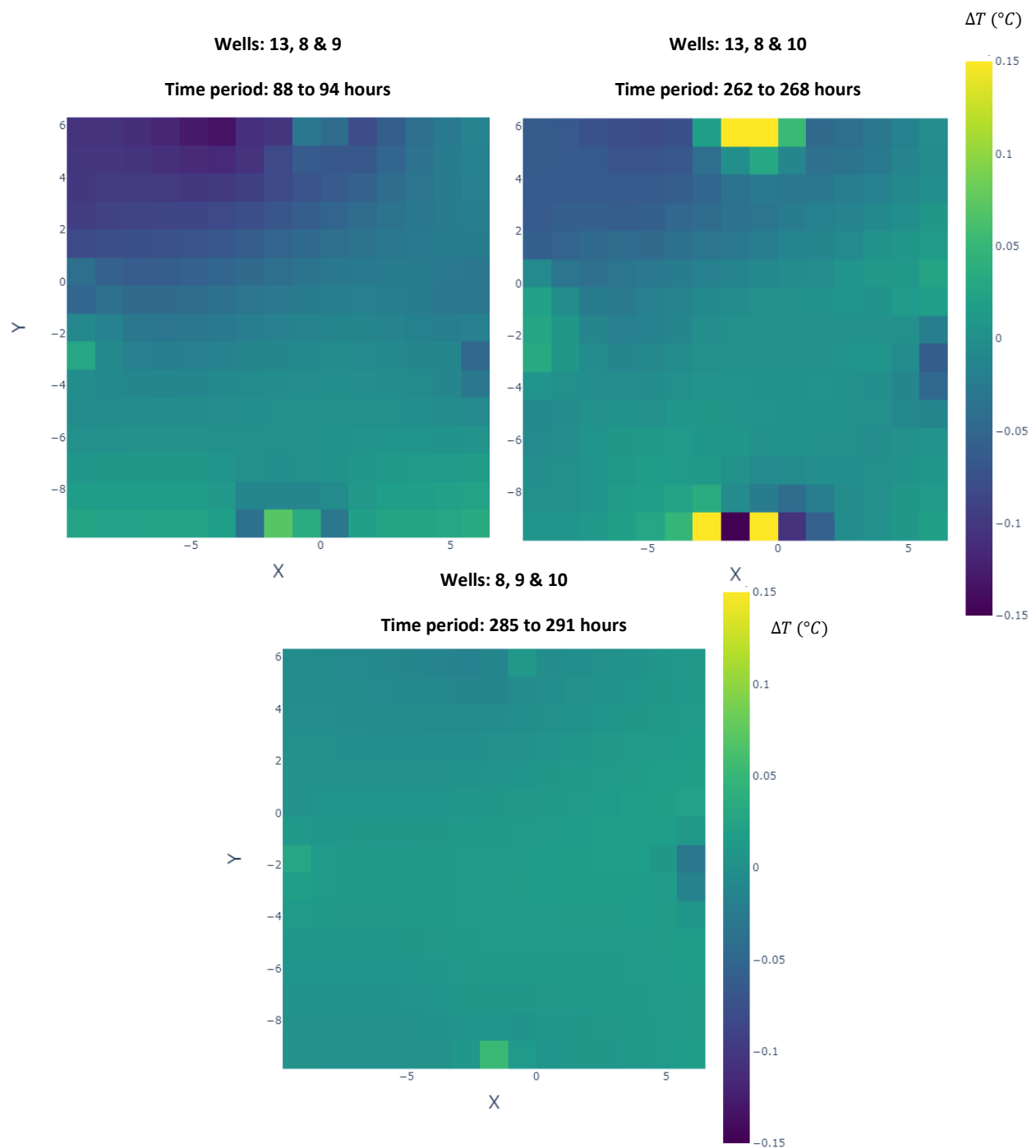
Figure 25: (a), up left: Temperature changes at depth 36.5m after 7 hours of wells 8, 9 and 13 extracting. (b), up right: Temperature changes at depth 36.5m after 7 hours of wells 8, 10 and 13 extracting. (c), bottom: Temperature changes at depth 36.5m after 7 hours of wells 8, 9 and 10 extracting.

At 36.5m depth, the temperature changes resulting from wells 8, 9 and 13 (Figure 25(a)) and 8, 10 and 13 (Figure 25(b)) are comparable again. The difference being that a larger drop in temperature is estimated for the first well combination. Changes are concentrated in the north-west of the section. For the third time, no temperature changes can be identified when only wells 8, 9 and 10 are operating. The final combination of wells was 8 and 10. However, similar to 8, 9 and 10 extracting, this

resulted in changes that were too small to be imaged with ERT data. For that reason, this combination is not addressed here.

3.4.3 Injecting at well 13

This section visualizes the temperature changes resulting from the injection of oxygenated water that is 1-2 degrees Celsius warmer than the in-situ groundwater. All images span a period of 62 hours.
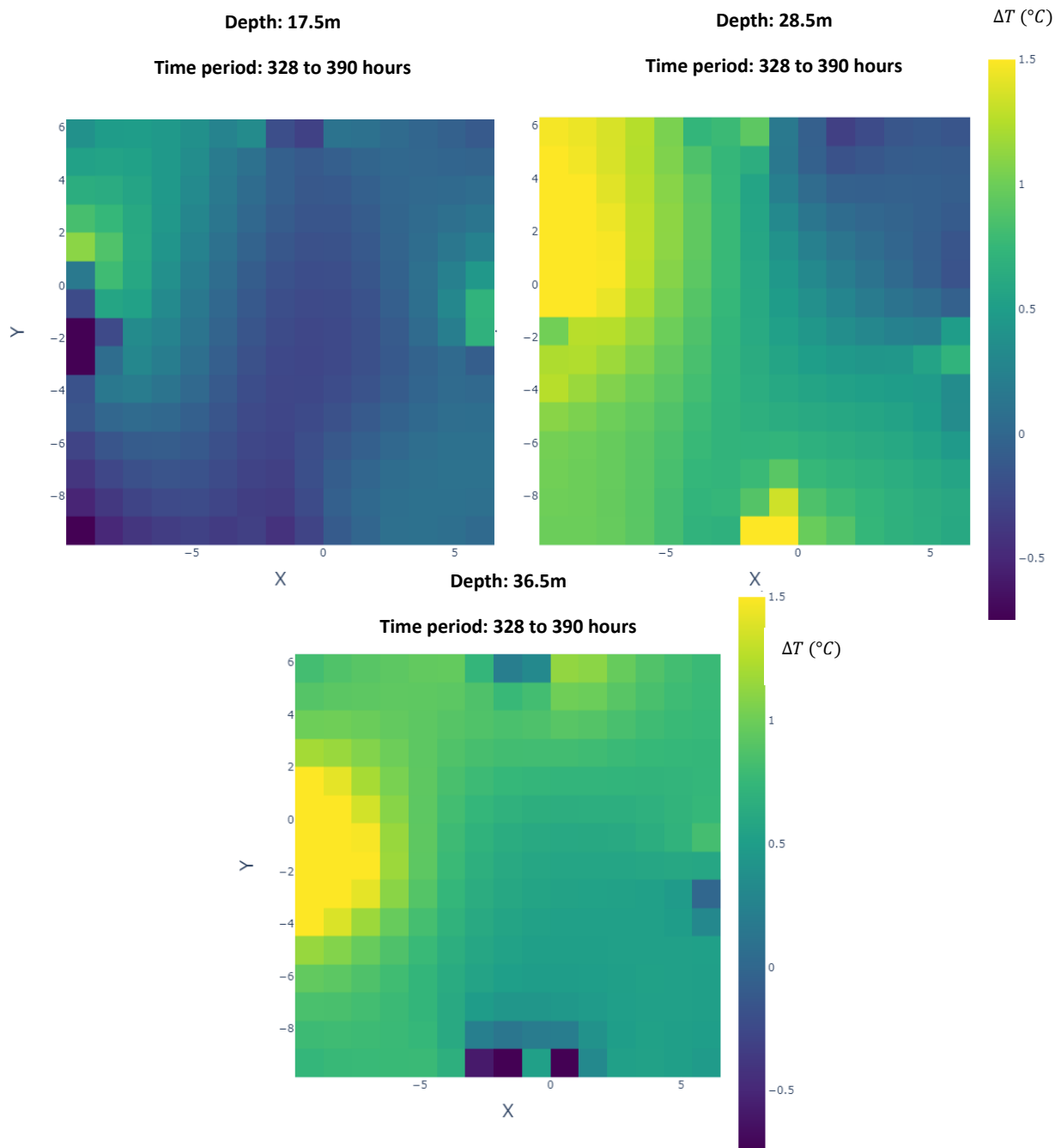
Figure 26: (a), up left: Temperature changes at depth 17.5m after 63 hours of wells 13 injecting oxygenated water. (b), up right: Temperature changes at depth 28.5m after 62 hours of well 13 injecting oxygenated water. (c), bottom: Temperature changes at depth 36.5m after 62 hours of well 13 injecting oxygenated water.

At a depth of 17.5 meter (Figure 26(a)), a general decrease in temperature is recorded after 62 hours of injecting. The maximum drop in temperature amounts to roughly 0.5°C, and is found around well

13, and to the south. The temperature scale is significantly larger than during the extraction phase to appropriately visualize the larger temperature changes induced by the injection of warmer oxygenated water. There seems to be a local increase in temperature of 0.5°C in the north-west. At 28.5m (Figure 26(b)) and 36.5m (Figure 26(c)) depth, increasing temperatures are noted, particularly in the north-west. In that region, they exceed 1.5°C. A difference between the two is that the temperature increase at 28.5m depth is generally larger; and concentrated on the west flank of the section. There is little to no change in the north-east corner. The temperature increase at 36.5m depth is seen all over the section.

3D Visualization

Now that 2D patterns at individual depths are identified, a (semi) 3D visualization serves to verify if these changes hold for the entirety of the respective depth region.

Figure 27 shows the resistivity converted temperature change with depth along the south-north (Figure 27(b)) and west-east (Figure 27(a)) axes. The temperature drop seen in the 2D analysis is evident in both sections from 10.5m down to 17.5 meters. The general temperature increases at depths 28.5m and 36.5m established earlier are also seen. In Figure 27(a) the higher temperature changes are again visible in the west, from depths of 20m down to 35m.
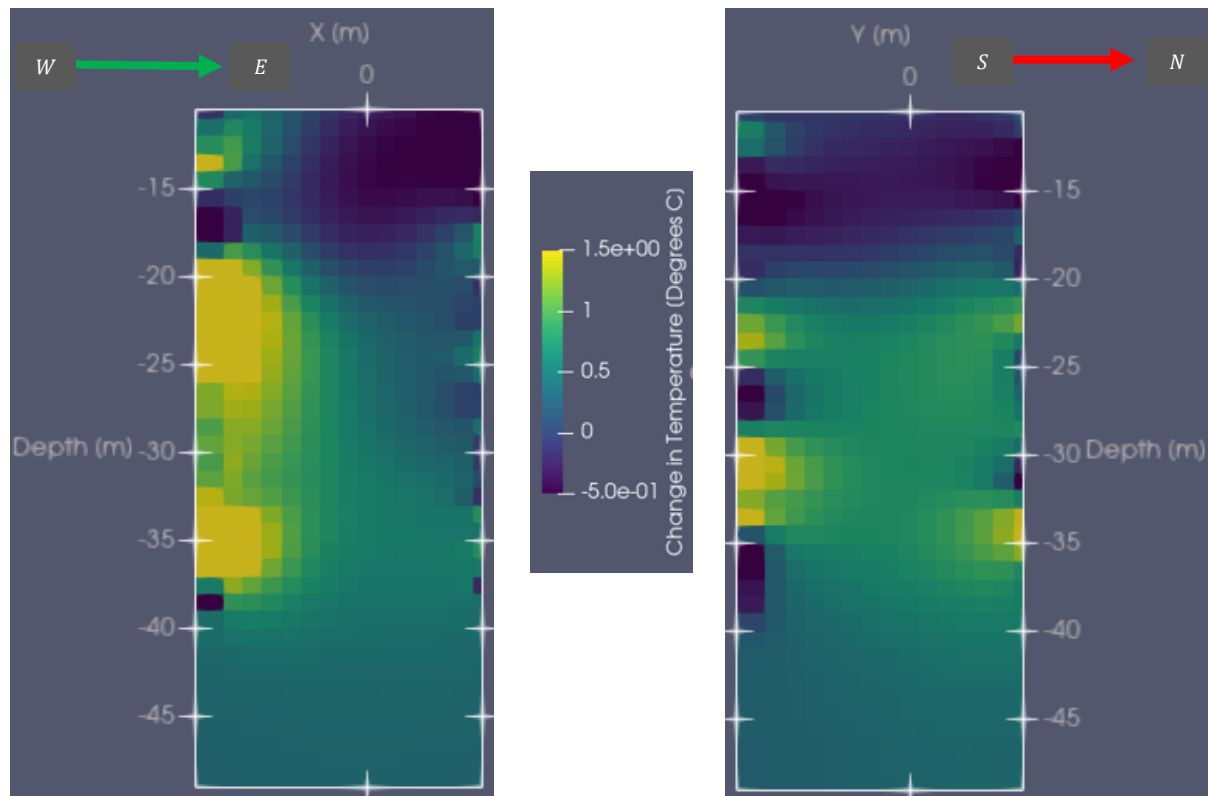
Figure 27: (a), left: CHERT imaging plane 2 (west-east) plotting changes in temperature with depth. (b), right: CHERT imaging plane 1 (south-north) plotting changes in temperature with depth. The changes are over a time period of 390 hours. The top 10.5 meters are cut off, as Hermans et al.'s (2014) model does not hold in the semi/unsaturated zone.

3D Glyph Analysis

Finally, a 3D glyph of the temperature changes in the studied volume is carried out and shown in Figure 28.

The glyph visualization presents the distribution of temperature changes in a 3D volume. It samples 5000 of the 11025 points, and assigns it an arrow size according to the magnitude of the value. The direction of the arrow holds no significance, other than conveying the sign of the temperature change.
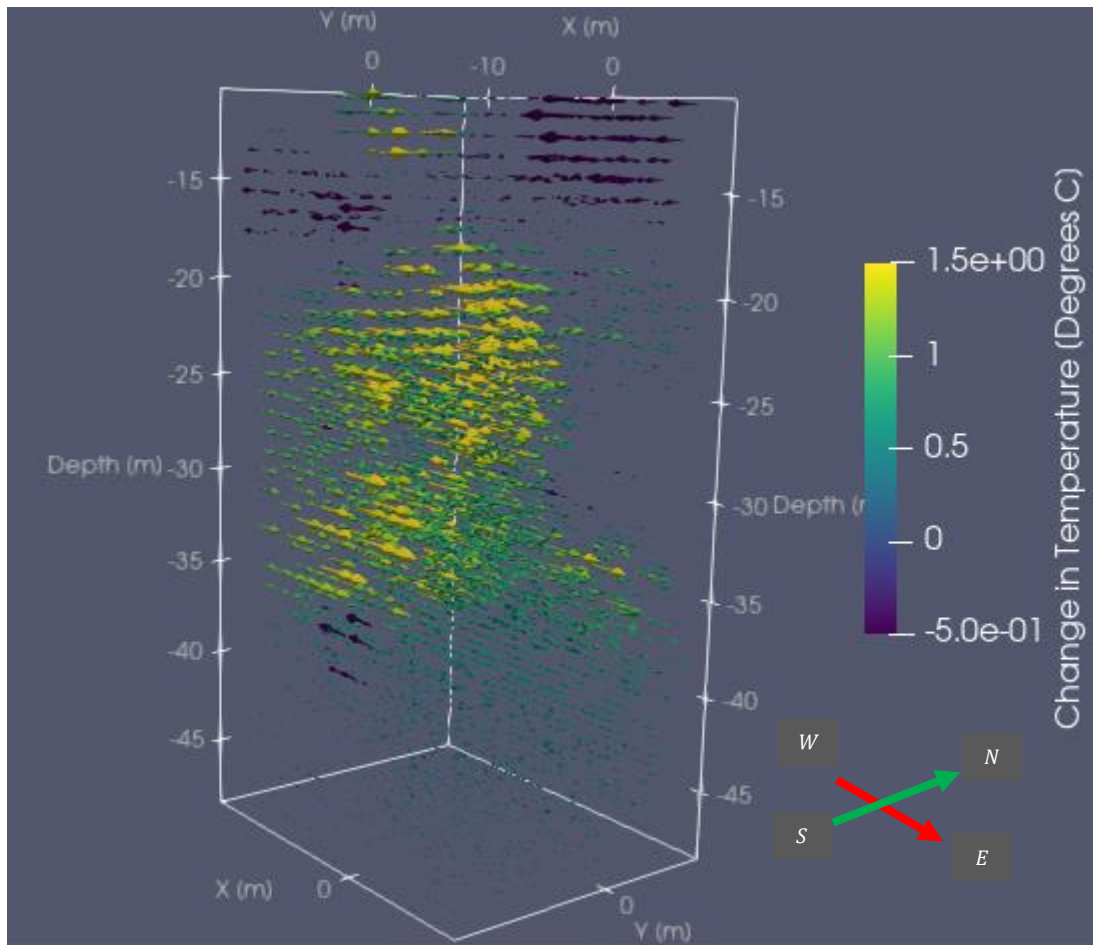
Figure 28: 3D Glyph visualization of the temperature changes over 62 hours of well 13 injecting oxygenated water. The size of the arrows shows the magnitude of the change in temperature. The arrows do not represent direction.

Figure 28 corroborates that the majority of temperature change occurs at depths between 20m and 35m. Within this region, high temperature change values are concentrated in the (north)west of the volume (negative x-coordinate, positive y coordinate).

4. Discussion

The ERT monitoring period can be split up into two phases: the groundwater extraction phase, and the 'warm' water injection phase. The extraction phase is used to visualize and explain the changes in the resistivity distribution resulting from different wells operating. The injection phase with its larger resistivity contrast is used to identify flow paths. Both are used to comment on the direction of groundwater flow. From the 1D analysis and a 3D visualization of results, the subsurface volume monitored by ERT was split up into 4 depth regions.

4.1 Extraction Phase

4.1.1 Depth Region 2: 17.5 meters

Discussion: A possible explanation is that, as pumping well 13 is extracting groundwater, water from the deeper regions of the aquifer is drawn upwards. Figure 8 showing the DTS data indicates that beyond 15 meters depth, the temperature of the subsurface increases at a rate of approximately 0.1 degrees Celsius per meter depth. Temperature changes estimated by the conversion of ERT data are in this order. Prior to extraction, the temperature profile is in equilibrium. This is disturbed during extraction. When the wells are stopped, and the updraw of warmer water halts, the equilibrium temperature profile is restored, likely through diffusion and/or influx of colder water driven by density differences and natural groundwater flow. If the subsurface was homogeneous and there was no groundwater flow, the region influenced by a vertical well screen would be cylindrical for the most part, with edge effects at the ends of the well screen. 17.5m is just above the start of the well screen (17.81m), but the resistivity change does form an elliptical pattern. The extent of resistivity change induced by the extraction of wells 8, 9 and 13 is stretched along the south-east north-west diagonal. From the hydrogeological study in Section 2, the groundwater flow was found to be in this direction. This stretching could therefore be an effect of groundwater flow.

By looking at the change in results when well 10 starts extracting and well 9 is off, the influence of wells far away from the ERT setup can be identified. Well 10 is positioned 100 meters to the south-west of the ERT setup, and well 9 is positioned 100 meters to the south-east. This geometry could explain the increase in resistivity in the south-west. At a sufficient distance from well 13, the effect of well 10 extracting groundwater could mitigate the updraw of warmer water with extraction. Closer to well 13 it appears that this updraw effect is enhanced.

4.1.2 Depth Region 3: 28.5 meters

Discussion: Overall, the resistivity response at 28.5m matches that seen at 17.5m. The drop in resistivity with extraction could therefore be attributed to the same mechanism of warmer water migrating upwards. Spatially, however, the changes are different. The effects of wells 8, 9 and 13 extracting are not exactly restored when the wells are off, which contrasts with the 2D slices at 17.5m and at 36.5 m. This can either be due to heterogeneity at this depth, or groundwater flow playing a larger role due to higher local velocities, or a combination of the two. Only heterogeneity seems unlikely however, as this should result in exact opposite resistivity response patterns when the wells are extracting and off respectively. This is the case in the other regions of interest. Groundwater flow velocity with depth can be checked using DTS derived groundwater velocity estimates. Physically, these results could suggest that, at this depth, the majority of water extracted originates from the south-east of the section, as this is the region that displays the most disturbance in resistivity.

When comparing the effect of wells 8, 9 and 13 with that of 8, 10 and 13, significant differences in the south-west and north-east regions are observed. This supports the previously established hypothesis

that this effect is the result of different faraway wells operating. As at 17.5m depth, the resistivity decrease in the vicinity of well 13 is slightly enhanced. The effect of well 10 extracting and well 9 off is more significant at 28.5m than at 17.5m. This could indicate that at around 28.5m, the subsurface (between well 13 and well 10) has larger horizontal permeability, possibly forming a preferential flow path.

Appendix 4 shows a 2D slice at a depth of -6.5m. It shows resistivity changes occurring in the shallow, semi saturated zone. It too seems to suggest that there is a difference between wells 8, 9 and 13 extracting water and wells 8, 10 and 13 extracting. The resistivity rise with the latter combination is slightly larger, in the west of the section.

4.1.3 Depth Region 4: 36.5 meters

Discussion: The well screen taking in groundwater ends at a depth of 32 meters. This can explain why the changes at 36.5m depth are not concentrated around well 13. Again, the effect of well 10 extracting and well 9 shut off perturbs the resistivity changes in the west of the section. However, having now considered all depths, it is evident that when only the far away wells operate, the ERT setup was unable to identify resistivity changes. Well 13 seems to be required to operate to see the impact of different wells, away from the ERT set-up.

The increase in resistivity at 36.5 meters depth with extraction is possibly the result of streaming currents induced by the upward flow of water. These should be present at all depths where capillary flow is happening but might be masked by the warm water updraw effect discussed earlier. There is no temperature data measured below 37m, but it is a possibility that the warm water updraw effect is minimal at 36.5m. This is just a theory however, and requires deeper temperature measurements and a possible quantification (or estimation) of the potential streaming current.

4.1.4 Considerations

The effects of different combinations of wells extracting groundwater are compared under the assumption that after the wells are turned off, the subsurface 'resets' to its initial state. As it is a dynamic medium, this is not always the case. Furthermore, the effect of faraway wells is challenging to isolate when their influence is minimal, particularly compared to that of well 13. During the 391 hours of ERT monitoring, there are limited combinations of wells operating, and different wells are almost always used in conjunction. This complicates characterizing the individual impact of wells further away from the ERT set-up.

ERT also has inherent uncertainty, as it provides an estimated resistivity model based on resistance measurements. This uncertainty is enhanced in the process of converting resistivity to temperature. For this reason this study refrains from making quantitative observations about the imaged temperature change distributions.

4.2 Injection Phase
4.2.1 Depth Region 2

Discussion: Figure 26(a) shows that after 62 hours of injecting warm oxygenated water, temperatures are estimated to decrease at a depth of 17.5 meter. Being just above the start of the well filter, this suggests that there is little to no upwards vertical flow here. Figure 27 and the glyph analysis suggest that this increase in resistivity (denoted as a drop in temperature) is relatively consistent for the entirety of this depth region. An exception is the decrease in resistivity in the north-west, which possibly represents a breakthrough from the injected water. In the glyph analysis, one can see that below 18 meters, consistent temperature increases are estimated. Above 18 meters, the opposite is

true. This supports the thesis that the injection of slightly warmer oxygenated water is indeed responsible for the observed decrease in resistivity.

4.2.2 Depth Region 3

Discussion: Influenced by the natural groundwater flow at 't Klooster, the majority of the injected warm water seems to flow to the north-west. This can explain the larger temperature increases estimated in those regions. This is supported by the glyph analysis and the 2D section. The area in the north-east of the 2D section at 28.5m depth displays little to no change with injection. This could be due to a local low permeability zone (for example: a boulder or clay lens). The glyph analysis shows that the largest temperature increases with injection are estimated in the (north)west of the region between 20m and 35m depth. Combined with the information from the 2D section at 28.5m, it can be hypothesized that this region represents a relatively horizontal flow path of warmer injected water. From the geologic study and Appendix 2, these depths are characterized by high permeability sandy gravels. This is a good conduit to flow and would allow for the lateral movement of groundwater.

The physical implications of these conclusions are that the region to the (south) east of well 13 receives less oxygenated water. From the extraction phase, the majority of extracted water at this depth is hypothesized to originate from the south-east. If this is the case, dissolved iron will break through to the well-screen faster, as the zone of oxygen rich water could potentially be limited in this direction.

4.2.3 Depth Region 4

Discussion: With injection, the estimated temperature pattern at 36.5m depth is similar to those seen in depth region 3 (Figure 26). Unlike at 28.5m depth, temperature increases are also estimated to be in the north-east. This supports that there might indeed be a localized low permeability region in the north-east at and around 28.5m. The deepest part of the well filter is positioned at 32.00m depth. The fact that significant temperature increases are estimated at depths up to 36.5m suggests that there is a significant degree of vertical flow from 32m down to 36.5m. Figure 27 and the glyph analysis show that beyond 36.5m, estimated temperature changes quickly diminish. At 40 meters, there is little to no discernable change in resistivity after 62 hours of injection, possibly marking the point where the Oosterhout formation transitions to very fine sands, significantly impeding both vertical and horizontal flow.

5. Conclusion and Recommendations

This research has demonstrated that ERT is adequately capable of imaging groundwater flow patterns resulting from the activity of groundwater extraction wells. Resistivity data collected over 390 hours at well field 't Klooster was converted to temperature values using Hermans et al.'s (2014) petrophysical model. DTS temperature measurements are used to corroborate the validity of this conversion. The activity of 4 groundwater wells extracting groundwater was correlated with changes in the estimated temperature data-set.

 A 1-D analysis at the midpoint of the ERT set-up identified 4 different depth regions that responded differently to the extraction and injection of ground water. To characterize the changes at each region, 4 representative depths were chosen. A 2-D analysis at these depths visualizing estimated temperature changes for different well combinations revealed horizontal differences in the response of the subsurface. A subsequent 3D glyph analysis and two orthogonal vertical sections plotting temperature change were done to combine the visualization of horizontal and vertical changes. It is hypothesized that wells 9 and 10 are able to influence the resistivity distribution at the ERT set-up,

despite being 100m removed. This is particularly so at a depths around 28.5m, suggesting a potential flow path at this depth. This is corroborated by the majority of temperature change occurring at and around these depths. The direction of temperature change seems to correspond with groundwater flow patterns, however, its effect cannot be isolated.

The following recommendations for improvements are linked to the uncertainties associated with the conclusions derived from this study:

1. Use an advanced hydrogeological flow model such as AMIGO to simulate the effect of extracting and injecting certain volumes of water for equal periods of time. This would give additional insight on the general direction of injected water, possibly confirming the flow path that was obtained from the ERT data. The current resolution of this model, at 25m x 25m is quite rough, however, macro-patterns should be identifiable.
2. Run a chemical model (or experiment) determining the effect of iron-ion removal on the electrical conductivity of the ground water. Comparing this with the effect of an increase of 1-2°C to assess the assumption that resistivity changes in the deeper subsurface are solely temperature dependent.
3. A future ERT survey could be designed around the operating schedule of the pumping wells. This can facilitate isolating the effect of single wells and the effect of groundwater. It could also be used to split up the survey time evenly over periods that different wells are operating. This is useful for checking if changes resulting from certain wells are consistent over different time periods.
4. To reduce uncertainties associated with ERT data, different geophysical monitoring tools such as borehole logs can be incorporated. It is also possible to determine flow velocities at DTS monitoring sites. These again would serve to reduce error in the data.
5. A quantitative analysis could be carried out. This requires rigorous error analysis to estimate the uncertainty associated with the ERT (and derived temperature) data.

6. References

Archie, G.E. (1942). The electrical resistivity log as an aid in determining some reservoir characteristics. Transactions of the American Institute of Mining and Metallurgical Engineers. 5. 1-8.

Braester, C., & Martinell, R. (1988). The Vyredox and Nitredox Methods of in situ Treatment of Groundwater. *Water Science and Technology, 20*(3), 149-163. doi:10.2166/wst.1988.0093

Cardarelli, E., & Donno, G. D. (2019). Advances in electric resistivity tomography: Theory and case studies. *Innovation in Near-Surface Geophysics,* 23-57. doi:10.1016/b978-0-12-812429-1.00002-7

Corwin, D., & Lesch, S. (2005). Apparent soil electrical conductivity measurements in agriculture. *Computers and Electronics in Agriculture, 46*(1-3), 11-43. doi:10.1016/j.compag.2004.10.005

Folmer, I. M., Herpen, F. V., & Krikken, A. (2012, December 11). *Gebiedsdossier Gelderland Winning 't Klooster* [PDF].

Geudens, P. G., & Grootveld, J. V. (2017, December). Dutch Drinking Water Statistics 2017. Retrieved from https://www.vewin.nl/SiteCollectionDocuments/Publicaties/Cijfers/Drinkwaterstatistieken-2017-EN.pdf

Grondwateronttrekking en - stroming. (n.d.). Retrieved June 16, 2020, from https://www.wrij.nl/statisch/baakse-beek/kopie-grondwater/stroming/

Günther, Thomas & Rücker, Carsten. (2012). Electrical Resistivity Tomography (ERT) in geophysical applications - state of the art and future challenges.

Halem, Doris & de Vet, Weren & Amy, G.L. & Dijk, J.. (2008). Subsurface iron removal for

drinking water production: Understanding the process and exploiting beneficial side effects.

Water Quality Technology Conference and Exposition 2008. 2802-2813.

Hayashi, M. (2004). Temperature-Electrical Conductivity Relation of Water for Environmental

Monitoring and Geophysical Data Inversion. *Environmental Monitoring and*

Assessment, 96(1-3), 119-128. doi:10.1023/b:emas.0000031719.83065.68

Hayley, K., Bentley, L. R., Gharibi, M., & Nightingale, M. (2007). Low temperature dependence

of electrical resistivity: Implications for near surface geophysical monitoring. *Geophysical*

Research Letters, 34(18). doi:10.1029/2007gl031124

Hermans, T., Vandenbohede, A., Lebbe, L., & Nguyen, F. (2012). A shallow geothermal

experiment in a sandy aquifer monitored using electric resistivity

tomography. *Geophysics, 77*(1). doi:10.1190/geo2011-0199.1

Hermans, T., Nguyen, F., Robert, T., & Revil, A. (2014). Geophysical Methods for Monitoring

Temperature Changes in Shallow Low Enthalpy Geothermal Systems. *Energies, 7*(8), 5083-

5118. doi:10.3390/en7085083

Hermans, T., Wildemeersch, S., Jamin, P., Orban, P., Brouyère, S., Dassargues, A., & Nguyen, F.

(2015). Quantitative temperature monitoring of a heat tracing experiment using cross-

borehole ERT. *Geothermics, 53*, 14-26. doi:10.1016/j.geothermics.2014.03.013

Huizer, S. (2019, April 19). *DRINKWATERWINNING 'T KLOOSTER* [PDF].

Iron & Manganese in Groundwater. (2007, February). Retrieved from

https://www.for.gov.bc.ca/hfd/library/documents/bib106076_iron_manganese.pdf

Jonge, M. D., Schoonenberg, F., Vries, D., & Hartog, N. (2018, March 14). IJzer- en

    mangaanverwijdering bij bereiding van drinkwater uit grondwater: Praktijk en modellering.

    Retrieved June 4, 2020, from https://www.h2owaternetwerk.nl/vakartikelen/ijzer-en-

    mangaanverwijdering-bij-bereiding-van-drinkwater-uit-grondwater-praktijk-en-modellering

Jonge, M. (2020). Pb. t Klooster.

[PowerPoint Slides]

Karaoulis, M., Tsourlos, P., Kim, J., & Revil, A. (2013). 4D time-lapse ERT inversion: Introducing

    combined time and space constraints. *Near Surface Geophysics, 12*(1), 25-34.

    doi:10.3997/1873-0604.2013004

Karaoulis, M., Bakx, W., Doornenbal, P., Kruiver, P., & Rijpkema, S. (2019). Visualising

    Groundwater Flow Using Time-Lapse Electrical Resistivity Tomography. *25th European*

    Meeting of Environmental and Engineering Geophysics. doi:10.3997/2214-4609.201902439

Karaoulis, M., Kim, J., & Tsourlos, P. (2011). 4D active time constrained resistivity

    inversion. *Journal of Applied Geophysics, 73*(1), 25-34. doi:10.1016/j.jappgeo.2010.11.002

Kim, J., Yi, M., Park, S., & Kim, J. G. (2009). 4-D inversion of DC resistivity monitoring data

    acquired over a dynamically changing earth model. *Journal of Applied Geophysics, 68*(4),

    522-532. doi:10.1016/j.jappgeo.2009.03.002

Labrecque, D. J., Morelli, G., & Lundegard, P. (1996). 3-D Electrical Resistivity Tomography For

    Environmental Monitoring. *9th EEGS Symposium on the Application of Geophysics to*

    Engineering and Environmental Problems. doi:10.3997/2214-4609-pdb.205.1996_079

Loke, M., Wilkinson, P., Chambers, J., & Strutt, M. (2013). Optimized arrays for 2D cross-borehole electrical tomography surveys. *Geophysical Prospecting, 62*(1), 172-189. doi:10.1111/1365-2478.12072

Maurer, H., Friedel, S., & Jaeggi, D. (2009). Characterization of a coastal aquifer using seismic and geoelectric borehole methods. *Near Surface Geophysics, 7*(5-6), 353-366. doi:10.3997/1873-0604.2009014

Multi-Phase Technologies. (2007). Retrieved July 26, 2020, from http://mpt3d.com/das1.html

Pierzynski, G. M. (2015, June 3). Soil: Earth's Largest Natural Filter. Retrieved from https://www.wqpmag.com/soil-earths-largest-natural-filter

Regberg, A., Singha, K., Tien, M., Picardal, F., Zheng, Q., Schieber, J., . . . Brantley, S. L. (2011). Electrical conductivity as an indicator of iron reduction rates in abiotic and biotic systems. *Water Resources Research, 47*(4). doi:10.1029/2010wr009551

Robert, T., Caterina, D., Deceuster, J., Kaufmann, O., & Nguyen, F. (2012). A salt tracer test monitored with surface ERT to detect preferential flow and transport paths in fractured/karstified limestones. *Geophysics, 77*(2). doi:10.1190/geo2011-0313.1

Gallagher, Neal. (2020). Savitzky-Golay Smoothing and Differentiation Filter.

Samouëlian, A., Cousin, I., Tabbagh, A., Bruand, A., & Richard, G. (2005). Electrical resistivity survey in soil science: A review. *Soil and Tillage Research, 83*(2), 173-193. doi:10.1016/j.still.2004.10.004

Schoonenberg, F. K. (2015). *Removing iron under anoxic conditions* (Unpublished master's thesis). Delft University of Technology.

Sharma, S. K. (2001). *Adsorptive iron removal from groundwater* (Doctoral dissertation,

    Wageningen University, 2001). S.I.: S.n.

Sheets, K. R., & Hendrickx, J. M. (1995). Noninvasive Soil Water Content Measurement Using

    Electromagnetic Induction. *Water Resources Research, 31*(10), 2401-2409.

    doi:10.1029/95wr01949

TNO-GDN (2020). Formatie van Kreftenheye. In: Stratigrafische Nomenclator van Nederland,

    TNO – Geologische Dienst Nederland. Geraadpleegd op 06-08-2020 op

    http://www.dinoloket.nl/stratigrafische-nomenclator/formatie-van-kreftenheye.

Van Ballaer, A. (2020, January 24). *Literature Review of Models Relating Electrical Resistivity*

    Tomography to Temperature [PDF]. Delft.

Vries, J. D. (n.d.). Groundwater. Retrieved May 4, 2020, from

    http://www.groundwatergovernance.org/fileadmin/user_upload/groundwatergovernance/

    docs/Hague/Readings/Groundwater_De_Vries.pdf

Wilkinson, P. B., Loke, M. H., Meldrum, P. I., Chambers, J. E., Kuras, O., Gunn, D. A., & Ogilvy, R.

    D. (2012). Practical aspects of applied optimized survey design for electrical resistivity

    tomography. *Geophysical Journal International, 189*(1), 428-440. doi:10.1111/j.1365-

    246x.2012.05372.x

Willemsen, J. (1998, September). *Water naar 't Klooster dragen* [PDF]. Doetinchem:

    Waterschap Rijn en IJssel.

Wraith, J. M., & Or, D. (1999). Temperature effects on soil bulk dielectric permittivity measured by time domain reflectometry: A physical model. *Water Resources Research, 35*(2), 371-383. doi:10.1029/1998wr900008

Zhou, B. (2019). Electrical Resistivity Tomography: A Subsurface-Imaging Technique. *Applied Geophysics with Case Studies on Environmental, Exploration and Engineering Geophysics*. doi:10.5772/intechopen.81511

7. Appendices

Appendix 1:

2016-2020	Redox	EGV	pH	CH4	Cl	NO3	SO4	HCO3	Fe	Mn	Ca	Mg	Na	K	NH4	TH	SI	Al	As	Cr	Ni
Putnaam		[mS/m]		[µg/L]	[mg/L]	[mg/L]	[mg/L]	[mg/L]	[mg/L]	[mg/L]	[mg/L]	[mg/L]	[mg/L]	[mg/L]	[mg/L]			[µg/L]	[µg/L]	[µg/L]	[µg/L]
HEK-P01-14	A	53	7.3	343	25	<	48	282	0.8	0.09	101	9	14	1.5	0.3	2.9	0.02	<	<	<	<
HEK-P02-15	A	59	7.2	18	28	1.0	65	298	0.0	0.12	110	11	17	2.9	0.2	3.2	0.0	<	<	<	2.0
HEK-P03-16	A	53	7.3	28	26	<	57	267	0.0	0.01	99	9	16	1.8	0.3	2.8	0.05	9.0	<	<	<
HEK-P05-10	A	61	7.2	127	26	<	67	311	0.3	0.05	115	10	16	3.2	0.3	3.3	0.01	<	<	<	2.0
HEK-P06-08	A	70	7.1	89	25	1.0	82	364	1.9	0.81	135	12	16	2.2	0.4	3.9	0.09	<	3.0	<	2.0
HEK-P07-09	A	59	7.2	143	28	<	62	304	0.2	0.07	113	9	15	5.1	0.4	3.2	-0.01	<	<	<	<
HEK-P08-11	A	55	7.2	130	27	1.0	52	288	0.2	0.02	105	9	14	3.0	0.3	3.0	0.02	3.0	<	<	1.0
HEK-P09-12	A	55	7.3	73	28	<	57	275	0.1	0.03	104	9	15	3.0	0.3	3.0	0.01	<	<	<	<
HEK-P10-13	A	54	7.3	135	28	3.0	58	266	0.1	0.02	103	9	16	1.8	0.3	3.0	-0.01	<	<	<	<
HEK-P11-17	A	56	7.2	143	26	<	54	288	0.3	0.14	105	9	13	3.3	0.3	3.0	0.02	<	<	<	<
HEK-P12-19	A	58	7.2	125	27	<	59	296	0.1	0.07	108	9	16	3.8	0.4	3.1	-0.03	<	<	<	<
HEK-P13-18	A	56	7.2	207	28	<	57	279	0.5	0.22	103	9	15	2.8	0.3	2.9	-0.01	3.0	<	<	<
Gemiddelde	-	57	7.2	130	27	2.0	60	293	0.4	0.14	108	10	15	2.9	0.3	3.1	0.01	5.0	3.0	<	2.0

Figure 29: Macroparameters 't Klooster wells from: Jonge (2020)

Appendix 2:
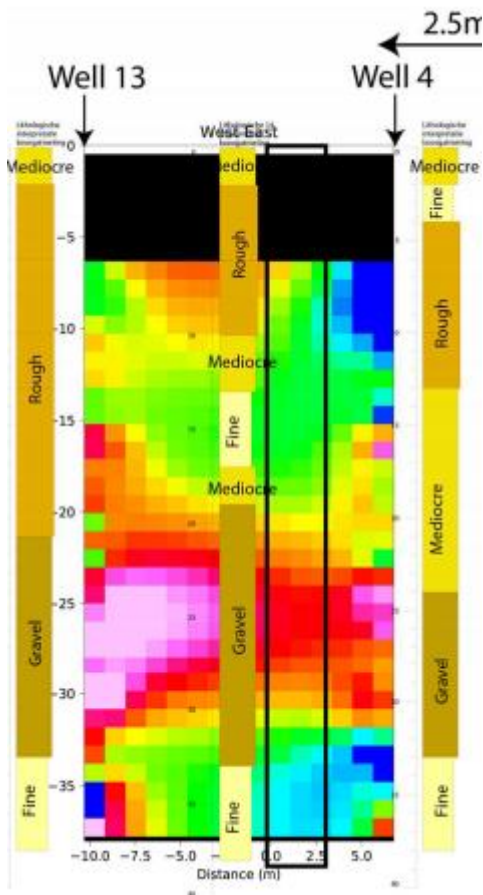
Figure 30: ERT, borehole logs and geology. From: Karaoulis et al (2020)

:

Appendix 3
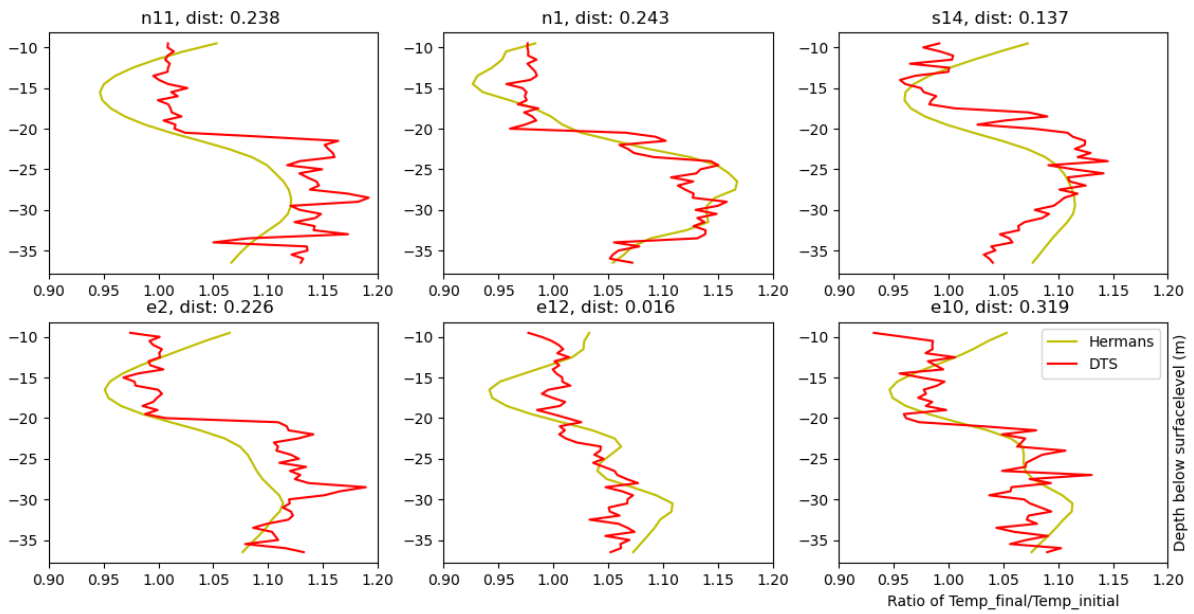
Figure 31: Plots showing the ratio of temperature before injection and after 62 hours of injection for unsmoothed DTS data, and resisistivity estimated temperatures.

Appendix 4

Wells extracting: 8, 9 and 13

Time period: 88 to 94 hours

Wells extracting: 8, 10 and 13

Time period: 328 to 390 hours
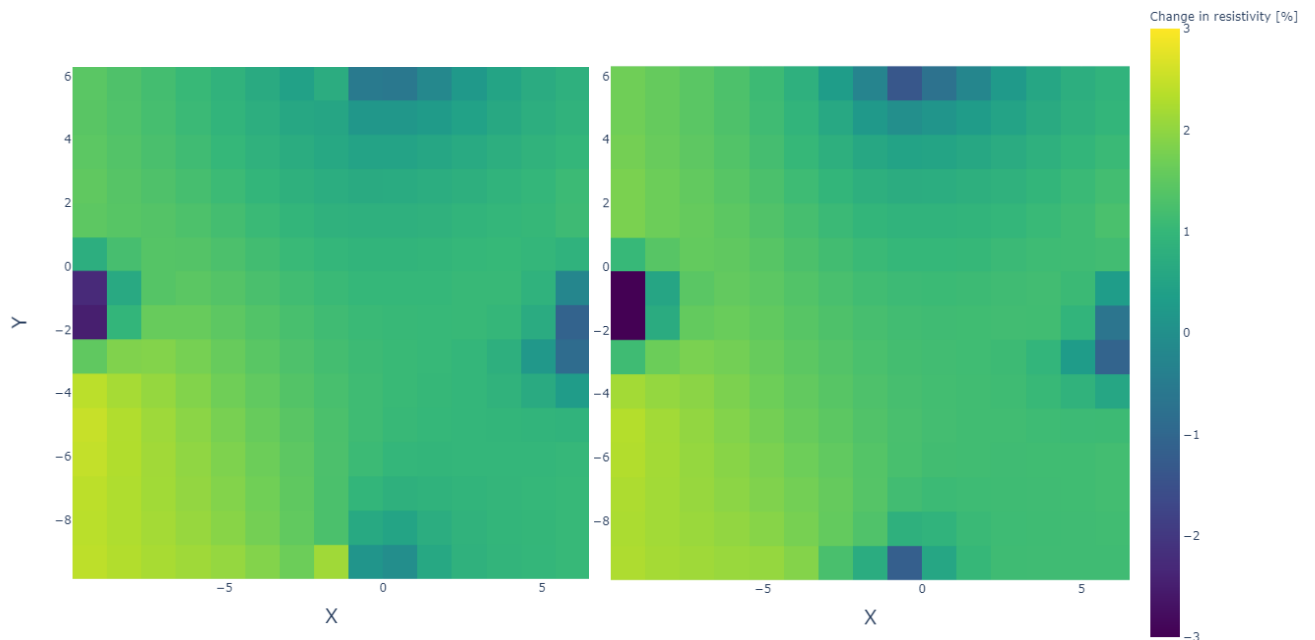
Figure 32: Graph showing % change in resistivity plots at a depth of 6.5 meters to show the difference of wells 8, 9 and 13 and well 8, 10 and 13 extracting groundwater.